


Intertwined crystal structure and electrical properties in layered battery materials $A_2Ni_2TeO_6$ ($A = Na/Li$)

B. Saha , A. K. Bera *, S. Kesari , and S. M. Yusuf 

*Solid State Physics Division, Bhabha Atomic Research Centre, Mumbai 400085, India
and Homi Bhabha National Institute, Anushaktinagar, Mumbai 400094, India*

 (Received 24 January 2023; revised 15 July 2023; accepted 19 July 2023; published 18 August 2023)

We report temperature evolution of the crystal structure and electrical properties, and their interconnection in the promising two-dimensional (2D) layered battery materials $A_2Ni_2TeO_6$ ($A = Na/Li$) by comprehensive neutron diffraction, Raman spectroscopy, and impedance spectroscopy studies. In this paper, we reveal that the crystal structures of Na- and Li-based compounds, with space group $P6_3/mcm$ and $Cmca$, respectively, have identical global crystal structures with alternating (Ni/Te) O_6 and alkali metal layers but with different internal structures of the alkali metal layers. Our soft bond valence sum analysis of the neutron diffraction patterns illustrates 2D conduction pathways within the ab planes for both compounds. Despite the Li ion having smaller size and lighter weight than that of the Na ion, our results reveal that the Na compound has higher ionic conductivity than the Li compound. By detailed crystal structural analysis, we divulge that the differences in the internal structures of the alkali metal ion layers, such as distance between the alkali metal ions, local crystal structural environment, and the relative site occupancies of the alkali metal ions, result in differences in the ionic conductivity. Additionally, in this paper, we demonstrate a correlation between crystal structure and electrical properties, where anomalies are found for both temperature-dependent electrical and local crystal structural parameters at ~ 475 – 575 K and ~ 200 – 300 K for Na- and Li-based compounds, respectively. In this comprehensive paper, we thus facilitate the understanding of the microscopic crystal structure, electrical properties, and their intercorrelations which are essential for the design and fabrication of highly efficient layered battery materials.

DOI: [10.1103/PhysRevMaterials.7.085001](https://doi.org/10.1103/PhysRevMaterials.7.085001)

I. INTRODUCTION

A transition from fossil fuels to environmentally friendly clean energy sources has made renewable energy one of the most important technologies in recent years [1]. Energy storage devices in the form of high-density rechargeable batteries are promising technologies for renewable energies [2,3]. Li- and Na-ion rechargeable batteries have been considered potential energy storage devices for small portable electronics (viz., mobile phones, laptops, or digital cameras) to large-scale grid energy storage devices. In this context, layered transition metal oxide compounds with intermediate layers of alkali ions (Li/Na) are important, as they show high ionic conductivity, high energy density, low dissipation energy, and improved alkali ion intercalation/deintercalation functionality due to lamellar structure [4–10].

A suitable electrode material should have high ionic conductivity with low dielectric loss for the transport of charge carriers as well as good electric conductivity to keep local charge neutrality. Therefore, the most fascinating task is to design adequate stable crystal structures that can contribute to a good electrical response with high dielectric constants while minimizing dielectric loss. Recently, the compounds

$A_2M_2TeO_6$ (where $A = Li, Na, \text{ and } K$, and $M = Co, Ni, Zn, Mg, \text{ and } Fe$) have been reported to show high ionic conductivity that is suitable for battery applications [11,12]. Among these, the Ni-based compounds with Na and Li ions, i.e., $Na_2Ni_2TeO_6$ (NNTO) and $Li_2Ni_2TeO_6$ (LNTO), exhibit high ionic conductivity, demanding to be potential candidates for battery applications [11]. Since the electrical properties of the battery materials are mostly governed by the underlying crystal structure and their stability, a detailed investigation of the microscopic crystal structural and electrical properties of $A_2Ni_2TeO_6$ ($A = Na/Li$) is required. In this paper, two isoformula compounds have been considered, where the structures of the magnetic layers are identical in both compounds, whereas the internal crystal structures of the alkali metal layers are different (Fig. 1). In NNTO, Na ions are distributed over three crystallographic sites, i.e., Na1, Na2, and Na3, with partial site occupancies. Na ions form NaO_6 trigonal prismatic coordination. On the other hand, LNTO has a single Li-ion site with LiO_4 tetrahedral coordination. The main motivation of this paper is to understand the role of the local crystal structure on the ionic conduction properties of the layered battery materials $A_2Ni_2TeO_6$ in general. By detailed crystal structural studies, employing neutron diffraction and Raman spectroscopy, we aim to bring out the underlying physics for differences in the conductivity with varying A ions.

In the recent past, the compound NNTO has been studied extensively for both battery as well as fundamental magnetic

*Corresponding authors: akbera@barc.gov.in;
smyusuf@barc.gov.in

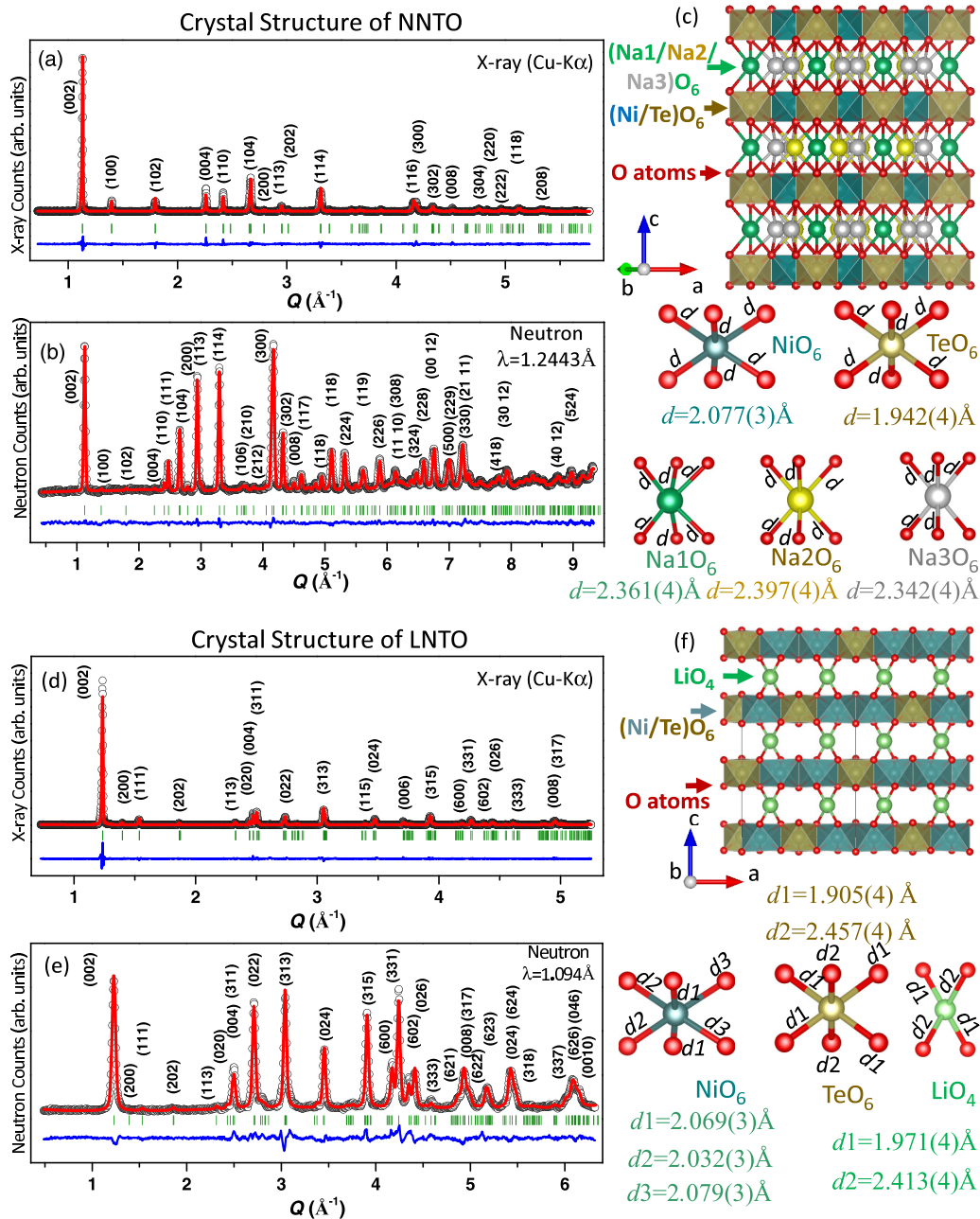


FIG. 1. Rietveld-analyzed room-temperature (a) x-ray and (b) neutron diffraction patterns, and (c) schematic of the layered crystal structure of NNTO. (d) X-ray and (e) neutron diffraction patterns, and (f) schematic of the layered crystal structure of LNTO. Experimental and calculated patterns are shown by the solid black circles and solid red lines, respectively. Blue lines at the bottom of each panel represent the difference between the experimental and calculated patterns. Vertical green bars denote the allowed Bragg peak positions.

properties [12–22]. The compound NNTO is reported to be a stable cathode material for a Na-ion battery [22]. The crystal structural stability during the intercalation/deintercalation processes is ensured by a rearrangement of Na ions among the three crystallographic sites. Such redistributions of Na ions prevent the crystal structure from collapsing during the intercalation/deintercalation processes [22]. The intercalation/deintercalation mechanism in NNTO is based mainly on the Ni-redox reaction [22] with a minor contribution from the oxygen reduction process.

A high ionic conductivity $\sim 10^1 \text{ Sm}^{-1}$ at 573 K, which is higher than several other Na-based honeycomb layered oxide

battery materials, is reported for NNTO [11]. For the ionic conduction, the closely packed honeycomb layers restrict the motion of the Na^+ ions along the c axis. The intermediate Na layers have chiral nuclear density distribution of Na ions. The chiral distribution of Na ions forms a closed loop, and it results in high ionic conductivity [15]. A similar type of Na-ion diffusion path has been reported for the $\text{Na}_{0.7}\text{CoO}_2$ compound [23,24]. In a molecular dynamics (MD) simulation [19], it was reported that the conduction of Na ions also depends on the concentration of Na ions as well as their relative distributions among the three crystallographic sites. The MD simulation also revealed that the hexagonal crystal

structure of the compound NNTO remains stable over the temperature range of 300–800 K [25]. In a recent temperature-dependent neutron diffraction study and bond valence sum (BVS) analysis of diffraction patterns, our group reported that the conduction in NNTO is governed by the site-specific Na-ion conduction pathways in the two-dimensional (2D) *ab* plane [13]. The conduction of the Na ions occurs through the Na1 (6g) and Na2 (4c) sites up to ~ 500 K. Above ~ 500 K, the Na-ion conduction occurs through all three Na ion sites Na1, Na2, and Na3 (2a). However, its crystal structure of hexagonal phase in the $P6_3/mcm$ space group remains stable up to 723 K [13]. Therefore, the observed different behavior in the ionic conduction pathways at ~ 500 K is expected to be governed by some changes in the local crystal structure. This motivates us to investigate the temperature evolution of the local crystal structural parameters, viz., bond lengths, bond angles, polyhedral distortions, and the distance between the Na^+ ions across this temperature (500 K). To further understand such electrostructural correlations, a comparative study on a similar compound is also essential; hence, two isoformula compounds NNTO and LNTO have been studied in this paper.

The compound LNTO has been studied mostly for its structural and electrochemical properties [11,26–29]. LNTO shows different crystal structural phases depending on the synthesis conditions, i.e., the layered phase (orthorhombic space group *Cmca*) in an ion-exchange reaction method and a disordered phase (orthorhombic space group *Fddd*) in the solid-state reaction method. Since our interest is on the layered compound, we have considered the layered LNTO with space group *Cmca* in this paper. For the electrochemical properties of LNTO, a recent report based on the density functional theory (DFT) calculations and experimental studies revealed a crystal structural phase transition during the deintercalation/intercalation of the Li^+ ions [27]. During intercalation/deintercalation process, the shifting of honeycomb layers leads to the structural phase transition. Here, the single crystallographic site for the Li ion could not prevent the crystal structural phase transition. Nevertheless, like NNTO, the intercalation/deintercalation process involves a redox reaction of Ni ions in LNTO as well. The layered LNTO exhibits a high ionic conductivity $\sim 10^{-2} \text{ Sm}^{-1}$ at 573 K, which is the highest among several other Li-based honeycomb layered oxides [11], however, smaller than that reported for the isoformula compound NNTO, having heavier and larger Na ions. This also motivates us to further investigate the origin of such discrepancies in the ionic conduction. Despite having high ionic conductivity, the temperature evolution of the crystal structure and its stability are unknown for these potential battery materials NNTO and LNTO.

In this paper, we have investigated the detailed temperature evolution of the crystal structures of the compounds NNTO and LNTO by comprehensive neutron diffraction and Raman spectroscopy measurements. The temperature-dependent local crystal structural parameters in terms of bond lengths and bond angles as well as polyhedral distortions associated with both compounds are derived. Detailed temperature-dependent electrical properties in terms of dc and ac conduction, dielectric constants, and electric modulus have been investigated by impedance spectroscopy. The role of the crystal structure on the electrical properties has been established for both

compounds. The nature of conduction pathways has been demonstrated for LNTO by soft BVS analysis of experimental neutron diffraction patterns and compared with that reported for NNTO. The results yield a detailed understanding of the electrostructural correlation of the high ionic conductive battery materials $A_2\text{Ni}_2\text{TeO}_6$ ($A = \text{Na/Li}$). This understanding will be useful for the design of the battery material and/or tuning their properties for suitable applications.

II. MATERIALS AND METHODS

Polycrystalline samples of NNTO were synthesized by the solid-state reaction method as reported in Ref. [13]. The polycrystalline samples of LNTO were obtained by an ion-exchange reaction method from NNTO. Here, LiNO_3 and the as-prepared NNTO (with weight ratio of 10:1) were mixed thoroughly and heated at 573 K for a period of 4 h for the ion-exchange reaction. The sample was then allowed to cool down to ambient temperature and washed with deionized water to dissolve residuals of LiNO_3 and NaNO_3 . Finally, the ion-exchanged LNTO yield was filtered from the solution. The completion of the exchange reaction was confirmed by x-ray diffraction where no residue of the peaks from the NNTO phase is found. Both Na- and Li-based samples are not air sensitive.

The crystal structural properties of NNTO and LNTO were investigated by using a laboratory source ($\text{Cu-K}\alpha$ radiation)-based x-ray diffractometer in Bragg Brentano geometry and the powder neutron diffractometers PD-I ($\lambda = 1.094 \text{ \AA}$) and PD-II ($\lambda = 1.2443 \text{ \AA}$) at Dhruva Research Reactor, Bhabha Atomic Research Centre, Mumbai, India. Temperature-dependent powder neutron diffraction measurements were carried out over 300–725 K for NNTO and over 5–300 K for LNTO. For the high-temperature neutron diffraction measurements on NNTO, a furnace was used. In this case, the powder samples were filled inside a quartz tube, which was then placed inside a vanadium can. The vanadium can was then attached to the sample stick of the furnace. The contribution from the sample environment (quartz tube, vanadium can, and the furnace) was estimated separately by an empty sample can measurement. The low-temperature neutron diffraction measurements on LNTO were carried out using a He4-based closed cycle refrigerator (CCR). In this case, each powder sample was filled directly in a cylindrical shaped vanadium container, and then the container was attached to the cold head of the CCR. The measured diffraction patterns were analyzed by using the Rietveld refinement technique by employing the FULLPROF computer program [30]. The ionic conduction pathways of LNTO were determined by the soft BVS analysis using the BondSTR program [31] available in the FULLPROF suite. The isosurfaces of the conduction pathways were plotted by using VESTA software [32].

The Raman spectra at various temperatures were recorded using a micro-Raman spectrometer (LabRAM HR800) with a temperature stage (Linkam THMS600). A 532 nm laser source of power 1 mW was used. The scattered light was resolved using 1800 lines/mm grating which gives a spectral coverage better than $0.5 \text{ cm}^{-1}/\text{pixel}$. The Raman spectra were analyzed by using Lorentzian peak functions.

Impedance spectroscopy measurements were performed on the disc-shaped pellets (having 10 mm diameters and thicknesses of 0.6 and 1.928 mm for NNTO and LNTO, respectively) using a commercial impedance analyzer PSM1735-NumetriQ (make: Newtons4th Ltd., UK) over the frequency (ν) range of 1–10⁷ Hz with an ac electric field amplitude of 0.2 V. The impedance spectra were recorded in the heating cycle over a temperature range of 98–623 K. A silver paste was uniformly coated on the flat sides of the pellets and dried before the recording of the impedance spectra.

III. RESULTS

A. Crystal structure at room temperature

The room temperature crystal structures of NNTO and LNTO have been investigated by combined analysis of x-ray and neutron diffraction patterns (Fig. 1). Here, NNTO crystallizes into a centrosymmetric hexagonal space group $P6_3/mcm$ (No. 193), having lattice parameters $a = b = 5.209(3)$ Å and $c = 11.155(9)$ Å. On the other hand, LNTO crystallizes into an orthorhombic structure with space group $Cmca$ (No. 64) having lattice parameters $a = 9.025(5)$ Å, $b = 5.171(3)$ Å, and $c = 10.207(9)$ Å. The crystal structural parameters for both compounds NNTO and LNTO, obtained from the Rietveld refinement of the neutron diffraction patterns, have been tabulated in Tables S1 and S2 in the Supplemental Material [33], respectively. The global crystal structures for NNTO and LNTO are the same, where both crystal structures consist of alternating layers of (Ni/Te)O₆ and Na/Li ions along the c axis. Moreover, within the (Ni/Te)O₆ layers, the Ni²⁺ ions form a magnetic honeycomb lattice with the nonmagnetic Te⁶⁺ ions at the centers of the hexagons for both compounds. However, there are several differences in their local crystal structure. In the case of NNTO, the NiO₆ and TeO₆ octahedra consist of six equal bond lengths of Ni–O [2.077(3) Å] and Te–O [= 1.942(4) Å], respectively (Fig. 1). However, in the case of LNTO, the Ni–O and Te–O bond lengths consist of three [2.032(3), 2.069(5), and 2.079(4) Å] and two [1.905(4), 2.457(4) Å] sets of unequal bond lengths (all values are in 300 K), respectively. Additionally, for NNTO, NiO₆ and TeO₆ octahedra contain four and three sets of unequal bond angles, respectively, whereas for LNTO, NiO₆ and TeO₆ octahedra contain seven and five sets of unequal bond angles, respectively (shown in the next section). The unequal bond angles (O–Ni–O)/(O–Te–O) within the NiO₆ and TeO₆ octahedra for both compounds lead to the octahedral distortions for both compounds NNTO and LNTO (discussed later in detail). Now we move to the alkali metal layer. In NNTO, Na ions are distributed over three Wyckoff positions: Na1(6g), Na2(4c), and Na3(2a), respectively, with partial site occupancies. The Na ions are located at trigonal prismatic coordination of oxygen atoms. All Na sites form three undistorted NaO₆ trigonal prisms of different bond lengths and bond angles. On the other hand, in contrast to NNTO with three Na sites, LNTO has a single Li-ion site (8e Wyckoff position). The internal structure of the Li-ion layer consisting of LiO₄ tetrahedra is different from that of the NNTO having NaO₆ trigonal prismatic coordination. This is because smaller Li⁺ ions are less favorable to occupy the trigonal prismatic sites [29,34]. The LiO₄ tetrahedra are distorted and consist of two unequal Li–O

bond lengths and two unequal O–Li–O bond angles. Therefore, the differences in the local crystal structural environments of alkali metals in NNTO and LNTO are expected to provide different electrical properties.

B. Temperature evolution of crystal structure

Neutron diffraction and Raman spectroscopy are the most effective techniques for studying the changes in local crystal structure, specifically oxygen octahedra and their arrangements [35,36]. Temperature evolutions of the crystal structures for the compounds NNTO and LNTO have been divulged through the combined study of neutron diffraction and Raman spectroscopy. For better comparison, the temperature-dependent neutron diffraction patterns (Fig. 2) and lattice parameters, bond lengths and bond angles (Figs. 3 and 4), Raman spectra (Fig. 5), and Raman shifts (Fig. 6) are plotted together for both Na- and Li-based compounds. Below, we discuss the temperature evolution of the crystal structures for the NNTO and LNTO one after the other.

1. Temperature evolution of crystal structure of NNTO

a. Neutron diffraction. The temperature dependence of neutron diffraction patterns for NNTO is shown in Fig. 2(a). All diffraction peaks could be indexed by space group $P6_3/mcm$ (No. 193) over the whole temperature region 300–725 K. The above observations indicate that the crystal structural symmetry remains invariant over the entire measurement temperature range up to 725 K. This agrees with the reported results of MD simulations, which revealed that the hexagonal crystal structure of NNTO remains stable over the temperature range of 300–800 K [25]. The detailed analysis of neutron diffraction patterns by the Rietveld method reveals anomalies in bond lengths and bond angles over ~475–575 K (Fig. 3): (i) sharp increase of all Na–O [Fig. 3(a)] and TeO₆ [Fig. 3(h)] bond lengths, but a sharp decrease of the Ni–O [Fig. 3(d)] bond length; (ii) sharp rise of the diagonal bond angles of NiO₆ octahedra toward 180° [Fig. 3(c)]; and (iii) decrease in the differences between three unequal O–Na–O bond angle values within the NaO₆ trigonal prism [Fig. 3(e)] and two in-plane O–Ni–O bond angle values of NiO₆ [Fig. 3(b)], but an increase in the difference between two in-plane O–Te–O bond angle values [Fig. 3(f)].

b. Raman spectroscopy. The peaks in the Raman scattering spectrum correspond to the resonance frequencies of vibrational modes in the material and can be described by $\omega = \sqrt{(k/m)}$, where k is the bond strength, and m is the reduced mass. The Raman mode frequencies are, therefore, strongly sensitive to any change in bond length and bond angle. Hence, Raman spectroscopy has been applied here to further probe the local crystal structural anomalies (without a phase transition).

Figure 5(a) shows the Raman spectrum of NNTO at 298 K, which contains 17 modes, and the spectrum matches well with the reported Raman spectra measured at room temperature [28]. As per the group theoretical calculations, a total number of 17 Raman modes are expected for NNTO with space group $P6_3/mcm$. Following the earlier report [28], the contributions of NaO₆ in the Raman spectrum appear at a lower frequency region of ≤ 350 cm⁻¹. On the other hand, the

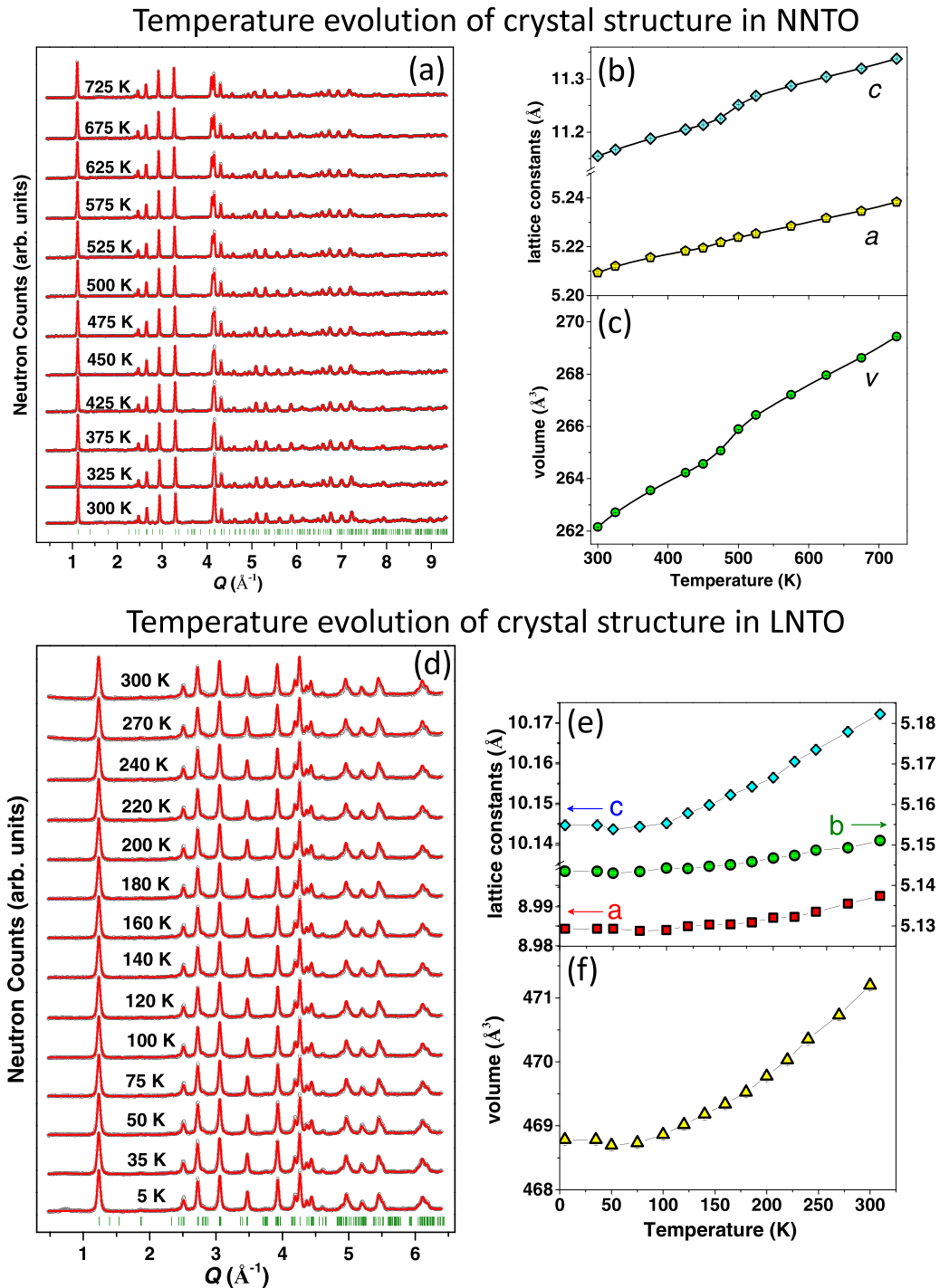


FIG. 2. Temperature dependent (a) Rietveld-analyzed neutron diffraction patterns, (b) lattice parameters, and (c) unit cell volume of NNTO over 300–725 K. Temperature-dependent (d) neutron diffraction patterns, (e) lattice constants, and (f) unit cell volume of LNT0 over 5–300 K.

contributions of $(\text{Ni/Te})\text{O}_6$ appear $> 350 \text{ cm}^{-1}$ in the Raman spectrum. The detailed assignments of the peak frequencies to the vibration modes are taken from the literature and given in Table S3 in the Supplemental Material [33]. The temperature evolution of the Raman spectra is shown in Fig. 5(c). In agreement with the neutron diffraction results, the temperature evolution of the Raman spectra also reveals anomalies in the resonance frequencies at $\sim 550\text{--}575 \text{ K}$, confirming the

local crystal structural anomalies. With increasing temperature from room temperature (298 K), all Raman modes show softening (i.e., decreasing in frequency) up to $\sim 550 \text{ K}$. Above $\sim 575 \text{ K}$, all weak Raman modes in the low-frequency side become broad. In the high-frequency region, the group of five intense peaks gradually merge with each other, which leads to a single broad peak over the frequency range of $630\text{--}700 \text{ cm}^{-1} > 575 \text{ K}$.

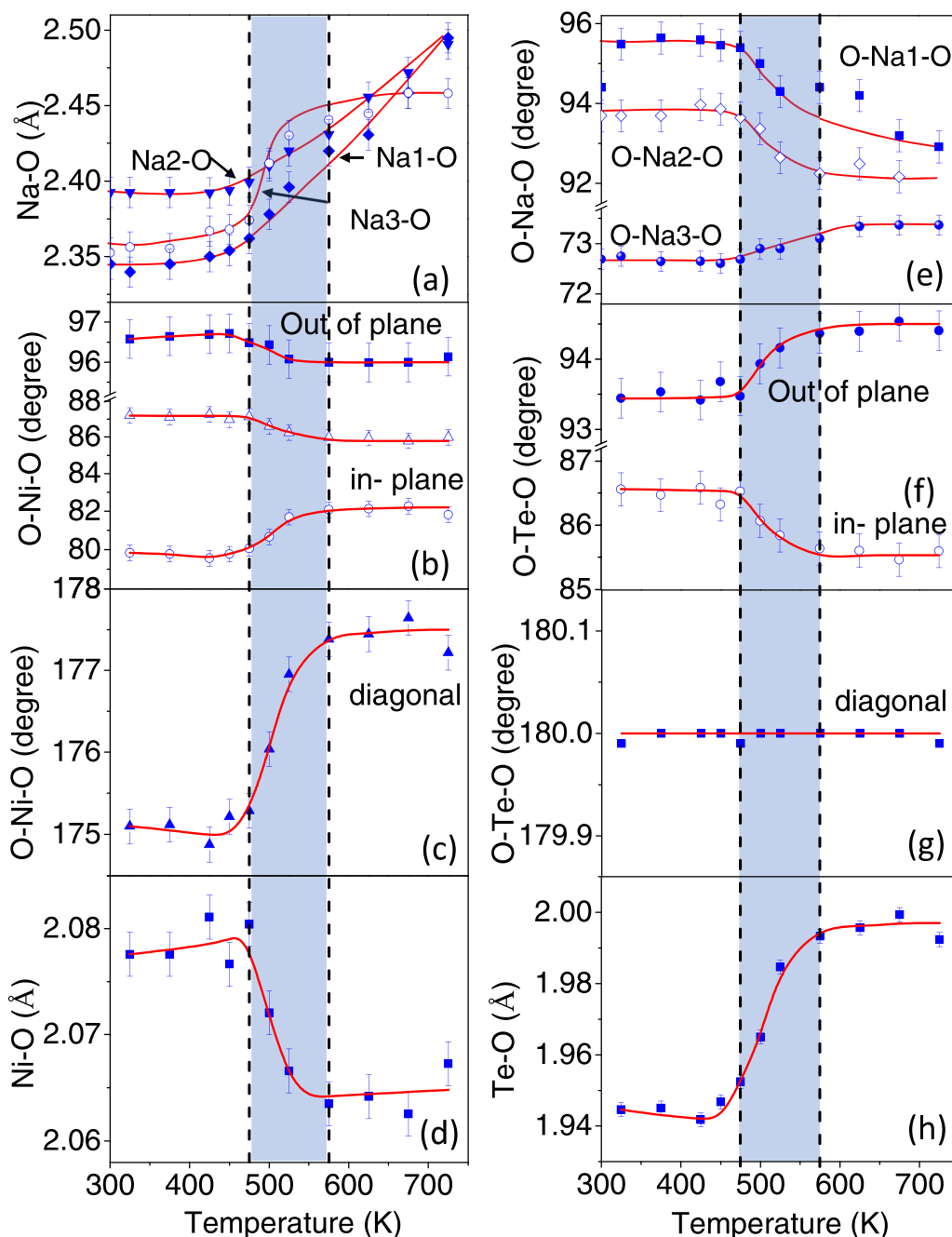


FIG. 3. Variation of bond lengths and bond angles as a function of temperature over 300–725 K for NNTO as derived from the analyses of neutron diffraction patterns. Solid lines are guides to the eye.

The variation of all Raman mode frequencies (determined by fitting each of the peaks of the vibrational modes in the Raman spectra with an individual Lorentzian peak function) as a function of temperature is shown in Fig. 6(a). All mode frequencies decrease linearly with the increase of temperature up to ~ 550 K and then show sharp anomalies over ~ 550 – 575 K. Additional Raman spectra were recorded in the interesting temperature range over 498–618 K with smaller temperature steps (Fig. S1 in the Supplemental Material [33]) to study the anomalies in details. The detailed temperature variations of the selected Raman mode frequencies are shown in Figs. 6(b)–6(g) over 450–620 K. All modes reveal anomalies

at ~ 550 – 575 K. Moreover, the other nonassigned vibrational modes also reveal anomalies at ~ 550 – 575 K (top panel of Fig. S2 in the Supplemental Material [33]). The temperature-dependent slope of Raman mode frequencies in the range 298–550 K are given in Table S3 in the Supplemental Material [33].

The results obtained from Raman spectroscopy [Figs. 6(b)–6(g)] are consistent with that observed in the neutron diffraction study (Fig. 3). The increase of Na-O bond lengths (as found in the neutron diffraction study) cause a decrease in the bond strength (k). As a result, the softening of the Na-O stretching mode at 263 cm^{-1} (shift toward the

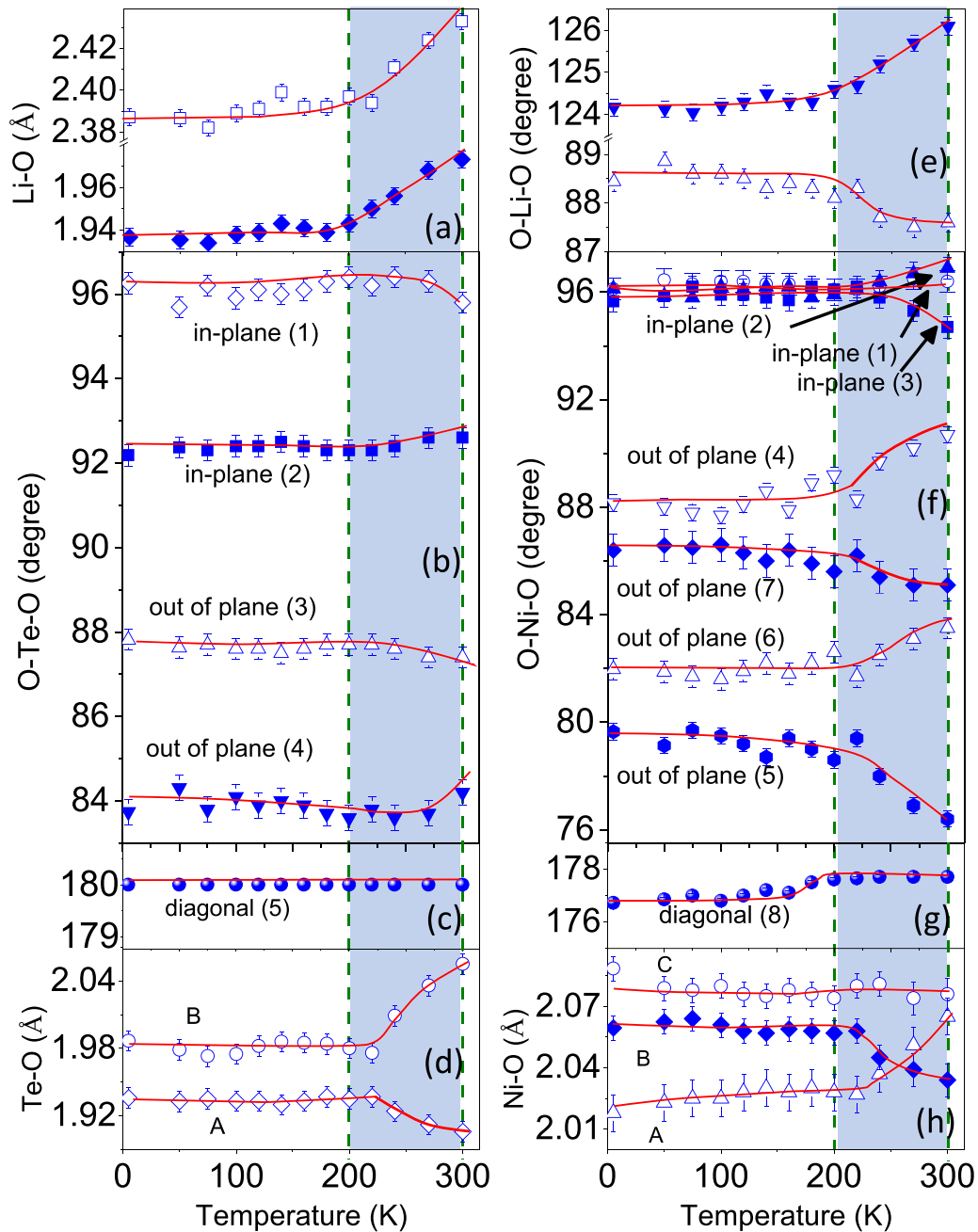


FIG. 4. Temperature variation of bond lengths and bond angles over 5–300 K for LNTO as derived from Rietveld analysis of neutron diffraction patterns. Solid lines are guides to the eye.

lower-frequency region) occurs. Similarly, the increase of the Te-O bond length leads to the softening of TeO₆ stretching modes at 377, 602, and 678 cm⁻¹. On the other hand, the decrease of Ni-O bond lengths causes an increase in the bond strength (*k*) and, hence, a hardening of the NiO₆ stretching mode at 640 cm⁻¹. Similarly, the bending modes (Fig. 6) are also in line with the results obtained from neutron diffraction (Fig. 3). The above correlations show excellent agreement between results obtained from neutron diffraction and Raman spectroscopy and confirm local crystal structural anomalies in terms of change in bond lengths and bond angles, keeping the global symmetry unchanged.

2. Temperature evolution of crystal structure of LNTO

a. Neutron diffraction. The temperature-dependent neutron diffraction patterns and the variation of the lattice constants are shown in Fig. 2(d). All diffraction peaks could be indexed by the orthorhombic *Cmca* (No. 64) space group over the entire temperature range of 5–300 K, revealing no crystal structural phase transition [Fig. 2(d)]. Small variations in the lattice constants (~0.22%, ~0.09%, and ~0.29% along the *a*, *b*, and *c* axes, respectively) and unit cell volume (~0.5%) are observed [Figs. 2(e) and 2(f)] over 5–300 K. Figure 4 depicts the temperature evolution of the bond lengths and bond angles which indicate anomalies over ~200–300 K. The

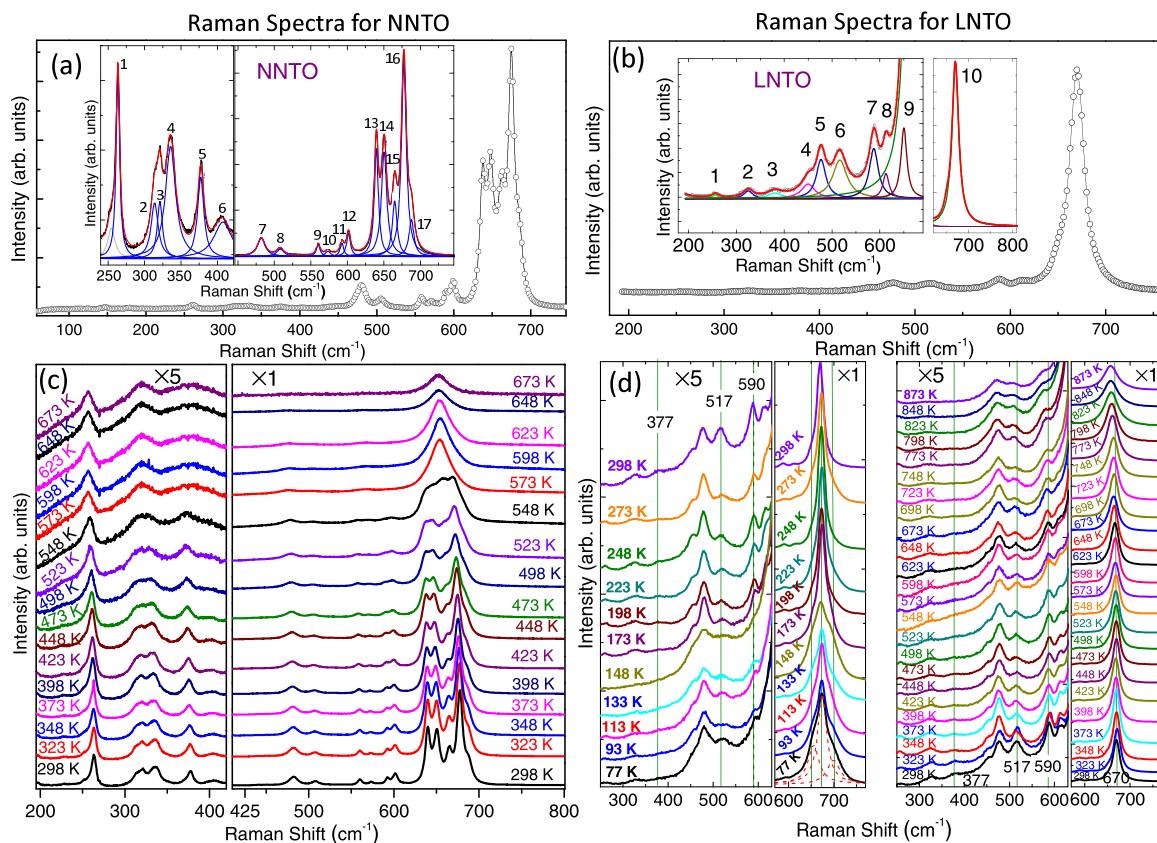


FIG. 5. Raman spectra measured at room temperature for (a) NNTO and (b) LNTO samples. Inset shows the fitting of individual Raman modes using Lorentzian line shapes. (c) and (d) Raman spectra as a function of temperature over (c) 298–673 K for NNTO and (d) 77–873 K for LNTO. For clarity, the low-frequency region (the left column) is zoomed 5 times. Red dashed lines in (d) are fitted Raman spectra at 77 K, revealing three peaks at 655.4, 674.4, and 700 cm^{-1} .

noticeable changes are (i) anomalies in the Li-O [Fig. 4(a)], Ni-O [Fig. 4(h)], and Te-O [Fig. 4(d)] bond lengths as well as O-Li-O [Fig. 4(e)] and O-Ni-O [Fig. 4(f)] bond angles and (ii) reduction in the differences between two in-plane bond angles (O-Te-O) [Fig. 4(b)] as well as two out-of-plane bond angles (O-Te-O) [Fig. 4(b)].

b. Raman spectroscopy. The Raman scattering spectrum of LNTO at room temperature (298 K) contains 10 peaks corresponding to different vibrational modes [Fig. 5(b)] which matches with the reported spectrum [28]. The observed 10 modes are much lower than the theoretically expected 30 modes (as expected for the orthorhombic $Cmca$ structure of LNTO) which may be due to either accidental degeneracy of phonon frequencies or weak undetectable intensity of a few modes because of weak polarizability due to weak dipole moments [37]. Following the assignments given in the earlier report [28] and like NNTO, the contributions from TeO_6 and NiO_6 appear at a higher frequency range ($>350 \text{ cm}^{-1}$) in the Raman spectrum, whereas the contribution from LiO_4 appears in the low frequency range ($\leq 350 \text{ cm}^{-1}$) in the Raman spectrum. The assignments of the modes are tabulated in Table S4 in the Supplemental Material [33]. The Raman scattering spectra of LNTO as a function of temperature, recorded over 77–873 K in the heating cycle, are shown in Fig. 5(d). At the lowest measured temperature of 77 K, the vibrational mode at 517 cm^{-1} , corresponding to TeO_6 bending, and the

three modes at 651, 670, and 700 cm^{-1} , appearing in the frequency range of TeO_6 symmetry stretching, reveal a distortion in the TeO_6 octahedra. With the increasing temperature, all three modes at 651, 670, and 700 cm^{-1} merge into one peak at $\sim 670 \text{ cm}^{-1}$ above $\sim 200 \text{ K}$. Similarly, the Raman mode at 590 cm^{-1} , corresponding to O-Ni-O stretching, becomes sharp with the increase of temperature from 77 to 298 K, suggesting that the NiO_6 octahedra also become less distorted. Further, upon increasing temperature from 298 to 873 K, all Raman modes move to the lower frequency (soften) and become broad.

The Raman shifts of all modes as a function of temperature for LNTO are shown in Fig. 6(h). All modes shift toward the lower frequencies with the increase of temperature. Figures 6(i)–6(n) highlight the variation of the selective Raman modes $\sim 200 \text{ K}$ associated with the stretching modes of Li-O and stretching and bending modes of NiO_6 and TeO_6 octahedra. In line with NNTO, all these modes reveal changes of slope at 200 and 300 K due to local crystal structural anomalies. Furthermore, other nonassigned vibrational modes also exhibit anomalies at ~ 200 and 300 K (bottom panel of Fig. S2 in the Supplemental Material [33]). All anomalies are also found in the cooling cycle of the measurements, revealing a reversible nature of these phenomena.

Like NNTO, the results obtained from the Raman spectroscopic study [Figs. 6(i)–6(n)] for LNTO are in line with

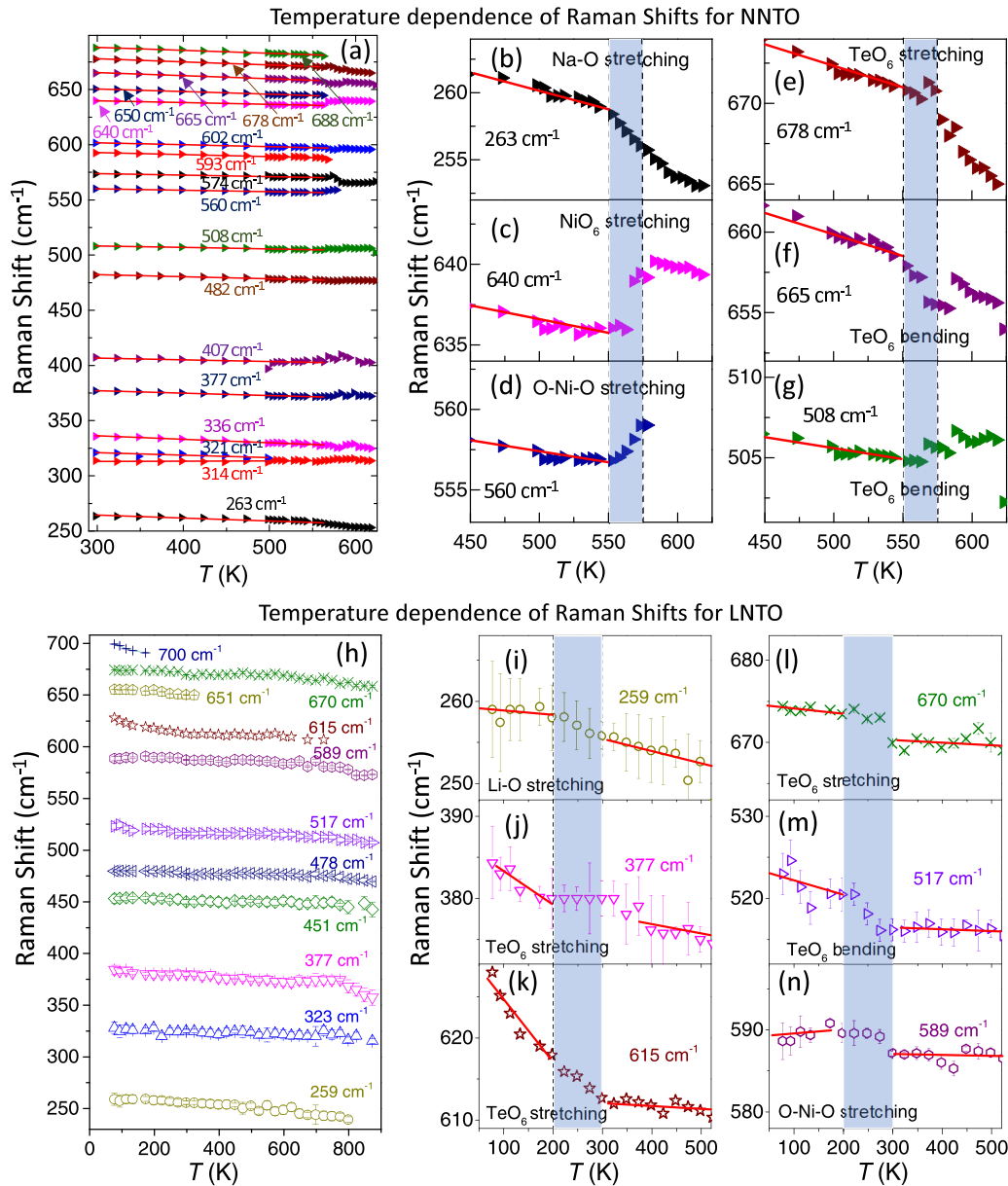


FIG. 6. (a) Temperature variation of Raman mode frequencies for NNTO. (b)–(g) Magnified view of Raman shift vs temperature curves for the selected vibrational modes associated with NaO_6 , NiO_6 , and TeO_6 octahedra stretching/bending. (h) Temperature variation of Raman mode frequencies of LNTO. (i)–(n) Magnified view of temperature-dependent Raman shift for selected vibrational modes associated with LiO_4 , NiO_6 , and TeO_6 octahedra. Solid symbols are experimental data, and red lines are linear fits.

that obtained from neutron diffraction (Fig. 4). The increase in the Li-O bond length results in a softening of the Raman mode at 259 cm^{-1} . Similarly, the changes in the Te-O bond lengths result in the observed anomalies in the Raman modes at 377 , 615 , and 670 cm^{-1} . Further, the anomaly in the TeO_6 bending is associated with the observed changes in the bond angle values. Similarly, the anomalies in the Raman modes associated with the NiO_6 octahedra are related to the change in the observed values of the Ni-O bond lengths and O-Ni-O bond angles. In summary, the results of neutron diffraction and Raman spectroscopy are consistent and reveal local crystal structural anomalies in LNTO without having any change in the global crystal symmetry, i.e., the space group symmetry.

The local crystal structural anomalies are pictorially illustrated in Fig. 7 for NNTO and LNTO. For NNTO, in a given Na layer, out of the three Na ions, the Na ion at the Na1 site moves toward the Na3 site, whereas the other two Na ion positions at the Na2 and Na3 sites remain unchanged. However, the Li position remains almost unchanged in LNTO. For NNTO, no significant movements of the Ni and Te ions are found in the transition metal ion layers, whereas a substantial movement in the Ni ions along the a axis is evident in LNTO. Most interestingly, the movements of oxygen ions are significant for both compounds. In the case of NNTO, within a given oxygen layer, the three oxygen ions connected with a Ni ion show synchronized movement in a circular

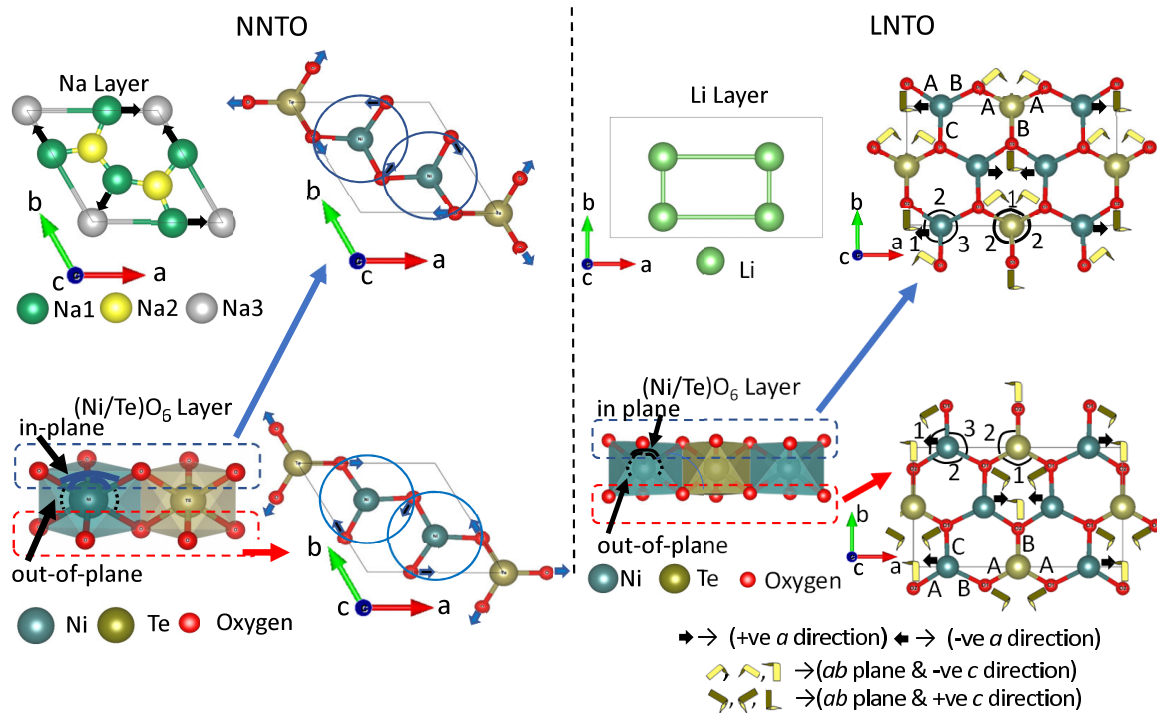


FIG. 7. Illustration of local crystal structural anomalies in NNTO across 500 K (left column) and in LNTO across 200 K (right column). Arrows represent movements of ions with increasing temperature across 500 K and 200 K for NNTO and LNTO, respectively.

fashion. Such circular motions are opposite for two adjacent Ni sites, i.e., clockwise and anticlockwise. Moreover, such oxygen movements in the adjacent oxygen layer are opposite. On the other hand, the movements of oxygen ions in LNTO occur along a , b , and c axes. Therefore, the natures of the local crystal structural anomalies are significantly different for NNTO and LNTO.

The local crystal structural anomalies are further shown in terms of the polyhedral distortions. The distortions are estimated from the differences in the values of bond angles as well as bond lengths for a given polyhedral type, i.e., NiO_6 , TeO_6 , and LiO_4 . For NNTO, with increasing temperature, the angular distortion $\Sigma = \frac{1}{12} \sum_{i=1}^{12} |\varphi_i - 90^\circ|$ reveals a sharp decrease of the distortion in NiO_6 but a sharp increase of the distortion in TeO_6 over 475–575 K [Fig. 8(a)]. Similarly, with the increase of temperature, for LNTO, the stretching distortion $\Delta = \frac{1}{6} \sum_{i=1}^6 \left[\frac{|d_i - d_{\text{mean}}|}{d_{\text{mean}}} \right]^2$ reveals a decrease of the distortion in NiO_6 but a sharp increase of the distortion in TeO_6 over ~ 200 – 300 K [Fig. 8(c)]. It may be mentioned here that the enhancement of the TeO_6 distortion for LNTO over 200–300 K is very significant. On the other hand, the change in the angular distortions (Σ) for NiO_6 and TeO_6 in LNTO is insignificant [Fig. 8(b)]. Now we compare the polyhedral distortions for the alkali metal ions layers. In contrast to undistorted NaO_6 trigonal prisms of NNTO, LiO_4 tetrahedral sites are distorted in LNTO due to unequal bond lengths as well as unequal bond angles. The stretching distortions (Δ) in LiO_4 remain almost unchanged [Fig. 8(b)], whereas the angular distortion (Σ) reveals an increase of the distortion in LiO_4 ~ 200 – 300 K with increasing temperature [Fig. 8(c)]. In summary, a significant change in the local crystal structure

occurs for both NNTO and LNTO over ~ 475 – 575 K and ~ 200 – 300 K, respectively.

The electrical properties are strongly related to the crystal structure; therefore, it is expected that the observed local crystal structural anomalies can affect the electrical properties. In view of this, we present next the temperature-dependent electrical properties.

C. Electrical properties

The electrical properties have been investigated by using frequency- and temperature-dependent impedance spectroscopy measurements. The recorded impedance data are analyzed to determine ionic conductivity, dielectric constant, and electric modulus.

1. NNTO

The temperature dependence of the real and imaginary parts of the impedance (Z), dielectric constant (ϵ), and modulus (M) parameters are shown in Figs. 9(a)–9(f) for selected frequencies. All these parameters show anomalies at ~ 593 K, which is related to the observed local crystal structural anomalies in terms of the change in the bond length and bond angle values as found from the neutron diffraction and Raman scattering studies. Further, a change of slope in the Arrhenius plots of ionic conductivity at ~ 550 K was also reported experimentally by Evstigneeva *et al.* [12] as well as theoretically (by MD simulation) by Sau and Kumar [25]. The above observations reveal coupling between crystal and electric degrees of freedoms in NNTO.

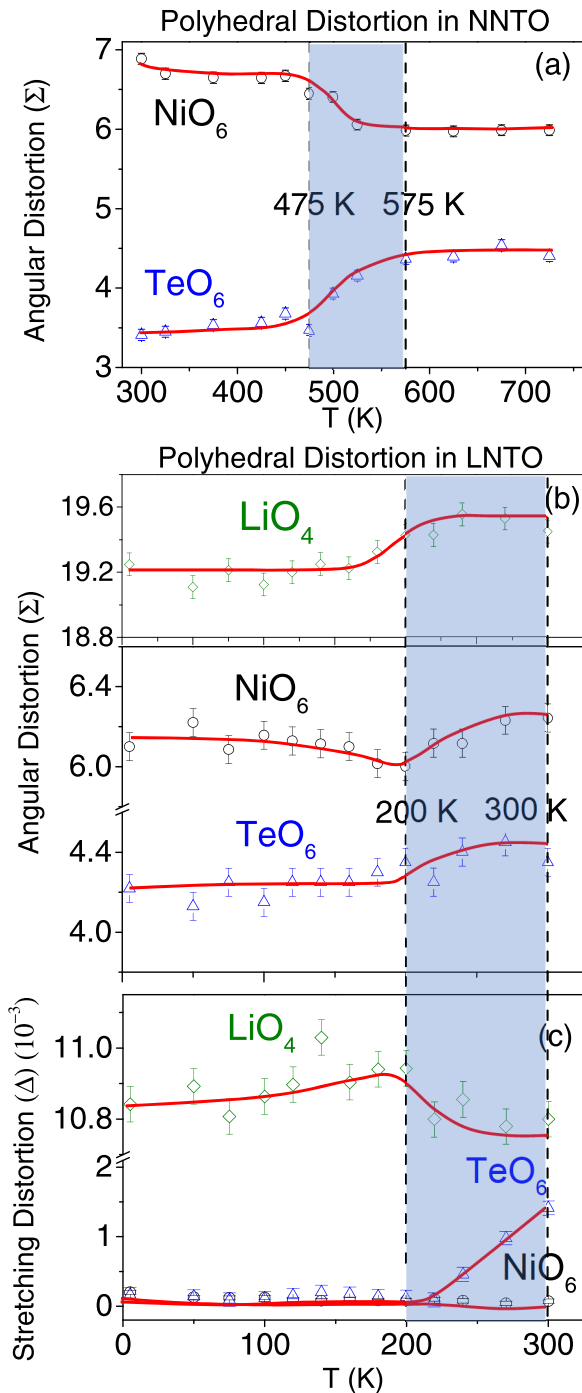


FIG. 8. Temperature evolution of angular distortions for (a) NNTO and (b) LNTO, and (c) stretching distortion for LNTO. Solid lines are guides to the eye. No polyhedral distortion is present for Na sites in NNTO.

The dielectric constant (ϵ') values are found to be high ($\sim 10^5$ to 10^8 for frequency 1 Hz) over the temperature range of 323–623 K. The observed higher ϵ' value for NNTO is comparable with LiFeO_2 ($\epsilon \sim 10^7$ at 573 K) [38] but higher than that for the other recently studied cathode materials LiNiPO_4 ($\epsilon \sim 10^4$ at 573 K) [39], $\text{LiFe}_{1/2}\text{Co}_{1/2}\text{VO}_4$ ($\epsilon \sim 10^5$ at 473 K) [40], $\text{LiNi}_{1-x-y-0.02}\text{Mg}_{0.02}\text{Co}_x\text{Zn}_y\text{O}_2$ ($\epsilon \sim 10^3$ at 393 K) [41], and $\text{K}_2\text{Ti}_4\text{O}_9$ ($\epsilon \sim 10^2$ at 773 K) [42]. The higher

value of dielectric constant can arise due to the conduction of ions in the grain interior as well as in the grain boundary, as reported in Ref. [43]. On the other hand, the value of dielectric loss ($\tan \delta$) is found to be low ($\tan \delta = 30$ at 300 K and 1 Hz) and comparable with that reported for other cathode materials, such as LiNiPO_4 ($\tan \delta \sim 11$ at 573 K) [39], $\text{LiFe}_{1/2}\text{Co}_{1/2}\text{VO}_4$ ($\tan \delta \sim 9$ at 473 K) [40], and $\text{K}_2\text{Ti}_4\text{O}_9$ ($\tan \delta \sim 3$ at 773 K) [42].

2. LNTO

The temperature dependence of ac conductivity for selected frequencies is shown as Arrhenius plots in Fig. 9(g). For 1 kHz, the curve increases monotonically with the increase of temperature up to ~ 200 K, then shows a plateau over ~ 200 – 300 K, and then shows a sharp rise > 300 K. With increasing frequency, the plateau in the conductivity vs temperature curve moves to a higher temperature. Above 300 K, a linear behavior in the Arrhenius plot of the conductivity curves [Fig. 9(g)] reveals a thermally activated conduction process in LNTO. Further, the Arrhenius plot of the dc conductivity curve, obtained from the Cole-Cole plot of the Z' vs Z'' curves, is shown in Fig. 9(h) over the temperature range of 300–773 K. The ionic conductivity values of $\sigma \sim 7.8 \times 10^{-6} \text{Sm}^{-1}$ at 313 K to $\sigma \sim 2 \times 10^{-1} \text{Sm}^{-1}$ at 773 K are found. An activation energy of $E_a = 0.261(4) \text{eV}$ has been determined from the linear fit to the Arrhenius plot.

The temperature-dependent real and imaginary parts of the dielectric constant ϵ' and ϵ'' curves show a gradual increase up to 200 K and then a sharp rise [Figs. 9(i) and 9(j)]. The ϵ' value is found to be very high $\sim 10^3$ to 4×10^5 over the temperature range of 100–473 K, which is in a similar range to that for NNTO. The inset of Fig. 9(j) shows the temperature-dependent dielectric loss factor ($\tan \delta$) at selected frequencies. The $\tan \delta$ value of LNTO is found to be ~ 5 at 300 K. The value is comparable with that of NNTO. The $\tan \delta$ vs T curves also show a plateau over ~ 200 – 300 K where the crystal structural anomalies were found. Figures 9(k) and 9(l) depict the variation of the modulus parameters as a function of temperature, which also show anomalies over ~ 200 – 300 K, consistent with the observed crystal structural anomalies from the neutron diffraction and Raman scattering studies. Therefore, a correlation between the crystal structure and electric properties is evident for LNTO as well.

D. Ion dynamics

The ion dynamics in the studied compounds have been investigated by an ac conductivity study. The real part of ac conductivity can be derived from the following equations:

$$\sigma' = (t/A)(Z'/(Z'^2 + Z''^2)), \quad (1)$$

where σ' is the real part of the ac conductivity, Z' and Z'' are the real and imaginary parts of the impedance, respectively, and the parameters t and A represent the thickness and the cross-sectional area of the pellets used for the study, respectively. The nature of the $\sigma'(v)$ curves can be normally expressed by Jonscher's power law, defined as $\sigma'(v) = \sigma'_{\text{dc}} + \alpha v^n$, where σ'_{dc} stands for dc conductivity, α is a prefactor denoting the polarizability strength of the hopping ions, and n is a frequency exponent representing the degree

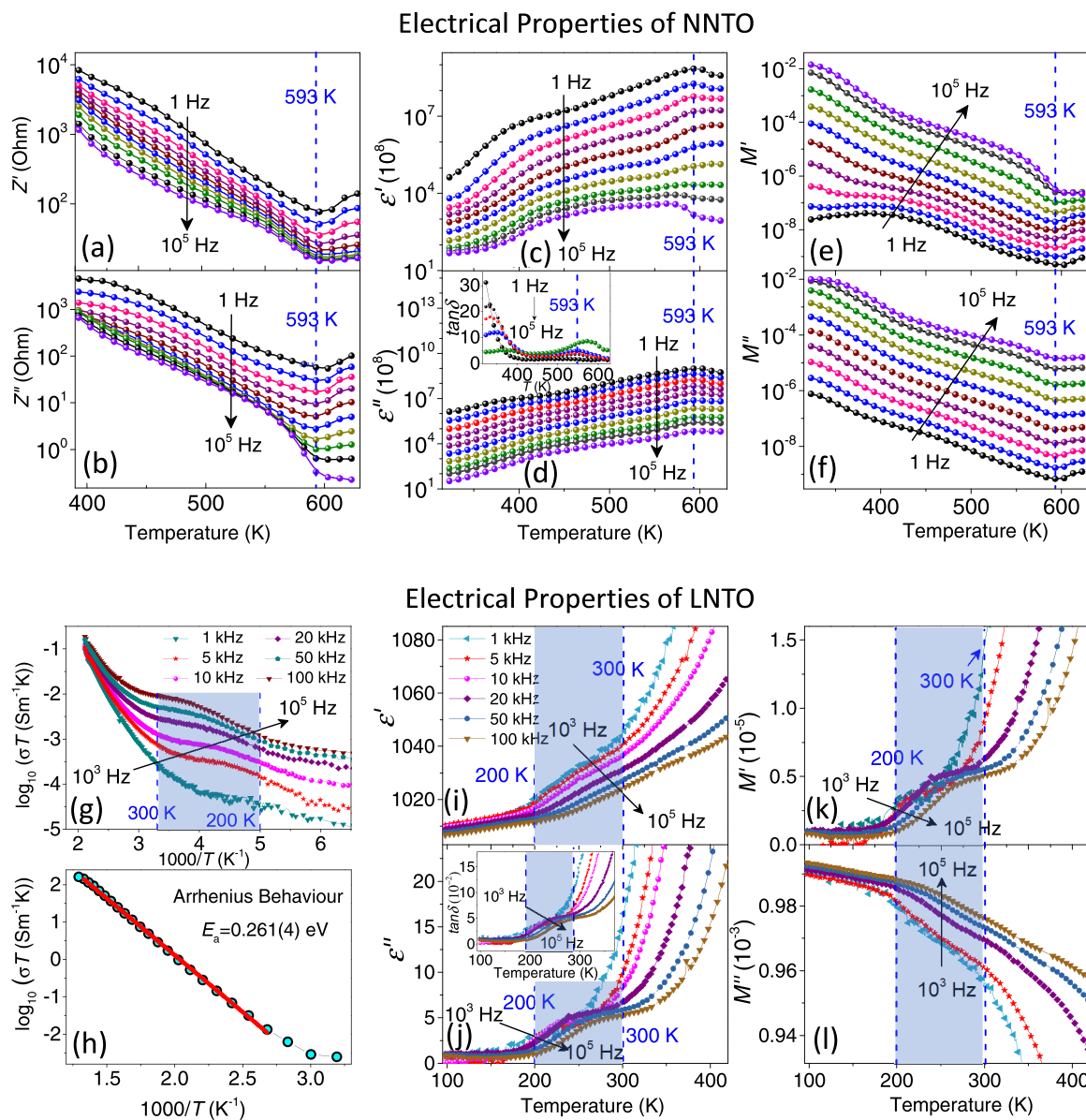


FIG. 9. Temperature-dependent (a) real (Z') and (b) imaginary (Z'') parts of complex impedance (Z); (c) real (ϵ') and (d) imaginary (ϵ'') parts of dielectric constant (ϵ); (e) real (M') and (f) imaginary (M'') parts of the electrical modulus parameter (M) for NNTO at selected frequencies. The inset of (d) shows the temperature dependence of dielectric loss factor ($\tan \delta$). Inverse temperature-dependent (g) ac conductivity; (h) Arrhenius plot of dc conductivity; (i) real (ϵ') and (j) imaginary parts (ϵ'') of dielectric constant (ϵ); (k) real (M') and (l) imaginary part (M'') of modulus parameter (M) for LNT0. The inset of (j) shows the temperature dependence of dielectric loss factor ($\tan \delta$).

of interactions of charge carriers with surrounding ions of the lattice [44]. The frequency exponent n values provide insight into the ionic conduction mechanism of the mobile ions.

I. NNTO

The frequency-dependent ac conductivity [$\sigma'(\nu)$] curves for the NNTO sample, derived from the impedance parameters (Fig. 9), are shown in Fig. 10(a). The $\sigma'(\nu)$ curves at low temperatures reveal a plateau over low frequencies and then increase with increasing frequency. At higher temperatures, the linear increase of the ac conductivity with increasing temperature can be attributed to the electrode effect as evident in the frequency-dependent impedance parameters

plot [Fig. 9(a)]. The derived frequency exponent n values [Fig. 10(b)] are found to decrease with increasing temperature. Such temperature dependence of n reveals that the Na-ion conduction occurs through a correlated barrier hopping (CBH) process [10].

The diffusion constant for the NNTO sample is calculated from the Nernst-Einstein relation [25,45]:

$$\sigma = \frac{nq^2D}{k_B T}, \quad (2)$$

where n denotes the number density of the alkali ions, q is the ionic charge (+1 for Na^+/Li^+) of the alkali ions, and D is the diffusion constant. Other symbols have their usual meanings.

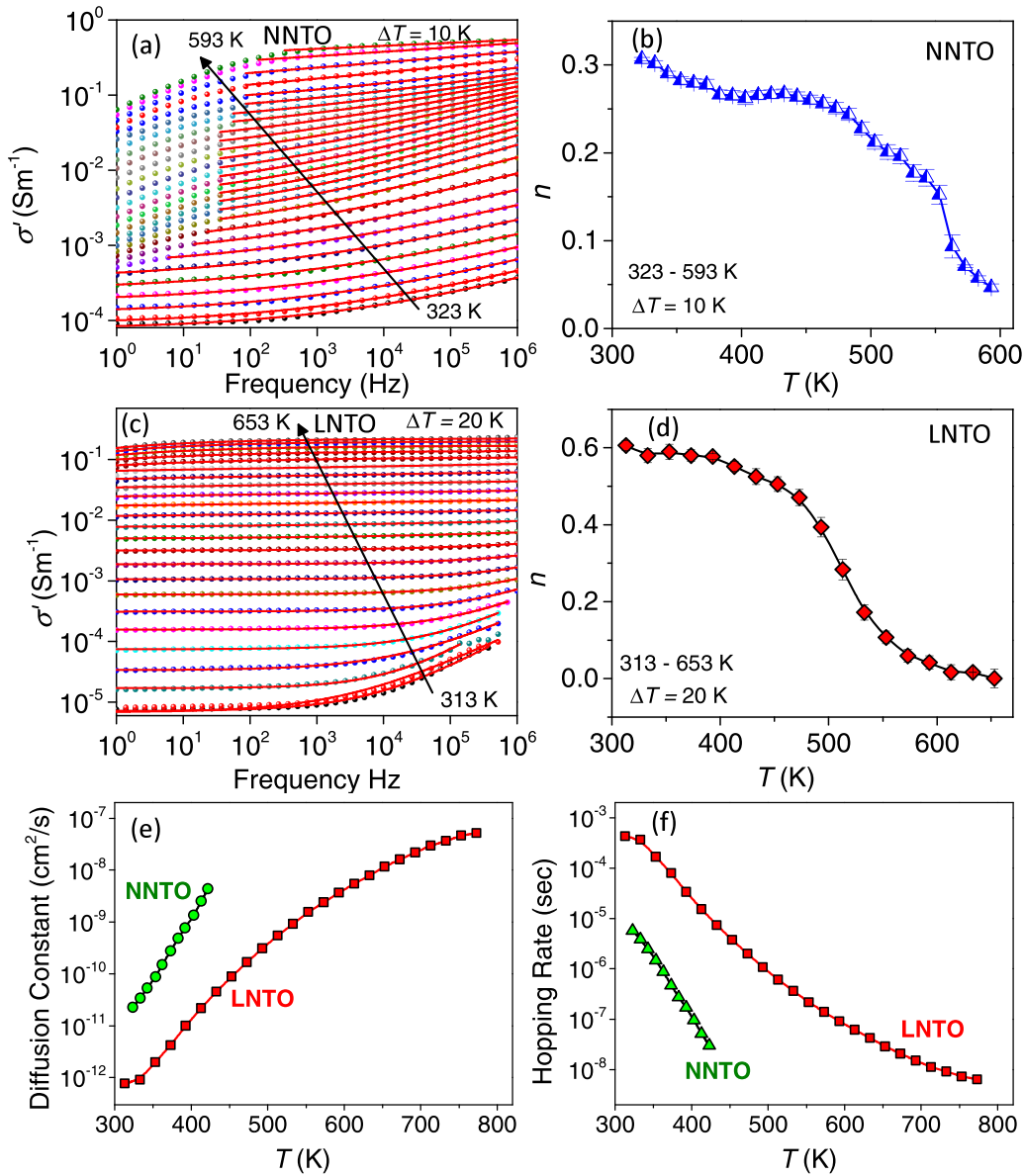


FIG. 10. Frequency-dependent ac conductivity (σ') curves fitted with Jonscher's power law for (a) NNTO and (c) LNTO. Temperature-dependent frequency exponent n value for (b) NNTO and (d) LNTO. (e) Diffusion constant and (f) hopping rates of ions for NNTO and LNTO.

The diffusion constant is found to be $\sim 2.28 \times 10^{-11} \text{ cm}^2/\text{s}$ at 323 K. With increasing temperature, the value of D increases by $\sim 10^2$ order and attains a value of $\sim 4.36 \times 10^{-9} \text{ cm}^2/\text{s}$ at 423 K [Fig. 10(e)]. The hopping rate of ions has been calculated by using the following equation [45]:

$$\Delta\tau = \frac{\langle l^2 \rangle}{2dD}, \quad (3)$$

where $\Delta\tau$ is the hopping rate of ions, $\langle l^2 \rangle$ is the mean square jump length, and d is the dimension of the diffusion system. Here, the hopping distance or the mean square jump length is the average distance between the neighboring Na-ion sites (discussed in detail in the Discussion section). The dimension of the diffusion is $d = 2$ due to 2D motion of the Na^+ ions (detailed discussion in the conduction pathways section). The

calculated hopping rate of ions is found to be $\sim 5.74 \times 10^{-6} \text{ s}$ at 323 K. The hopping rate decreases with increasing temperature and becomes $\sim 3 \times 10^{-8} \text{ s}$ at 423 K [Fig. 10(f)], suggesting a faster ionic motion at high temperature.

2. LNTO

The $\sigma'(v)$ curves for the LNTO sample are shown in Fig. 10(c). Here, the $\sigma'(v)$ curves reveal a plateau for low frequencies and then increase with increasing frequency. The derived n values [Fig. 10(d)] obtained from the fitting of Jonscher's power law depict a decreasing nature with the increase of temperature, like that for NNTO, revealing that the Li-ion conduction occurs in LNTO through the CBH process.

The diffusion constant and hopping rate of ions of LNTO have been estimated as for NNTO. The value of the

diffusion constant is $\sim 7.76 \times 10^{-13} \text{ cm}^2/\text{s}$ at 313 K, which increases with the increase of temperature and reaches $\sim 5.22 \times 10^{-8} \text{ cm}^2/\text{s}$ at 773 K [Fig. 10(e)]. The hopping rate of ions is found to be $\sim 4.3 \times 10^{-4} \text{ s}$ at 313 K, which decreases with increasing temperature and becomes $\sim 6.41 \times 10^{-9} \text{ s}$ at 773 K [Fig. 10(f)]. The decrease of the hopping rate suggests a faster ionic motion at high temperature. Figures 10(e) and 10(f) reveal that the diffusion constant is large for NNTO as compared with that for LNTO. It is also apparent that the hopping rate is faster in NNTO than that for LNTO.

Further, according to the jump relaxation model [46], the n value represents the ratio of the back-hop rate to the site relaxation rate. The lower n value at the high-temperature region can be attributed to the slower back-hop rate than the site relaxation rate. The slower back-hop of the charge carriers at the higher-temperature region leads to weaker interaction of the Na/Li ions with the surrounding ions, resulting in an enhancement of the translational motion/conduction of Na ions.

It is to be mentioned that, in the CBH process, ionic conduction occurs by surpassing the activation energy through a hopping mechanism. In the present case, both studied compounds reveal a deficiency of alkali ions, setting the ground for the hopping process (elaborated in the Discussion section). With the reduced Na^+ -ion concentration, additional vacant sites are formed within the systems. These additional

vacant sites decrease the interaction between the mobile Na^+ ions, leading to a reduction in activation energy [47–50]. As a result, the deficiency of alkali ions generates additional pathways for ionic conduction, facilitating a higher ionic conductivity.

E. Illustration of conduction pathways (BVS)

To elucidate the Li-ion conduction pathways in LNTO, soft BVS analysis [51–53] has been performed. The Li-ion conduction pathways are determined from the atomic positions obtained from the Rietveld analysis of the room-temperature neutron diffraction pattern [Fig. 1(e)]. In this method, the accessible sites for the Li ions are calculated by considering Pauling's rule, which states that the sum of all bond valences surrounding an atom should be the atomic valence as follows:

$$V_i = \sum s_{ij} = \exp\left(\frac{R_0 - r_{ij}}{b}\right), \quad (4)$$

where V_i represents the valence state of the i th atom, and s_{ij} and r_{ij} represent the valence and bond length between the i th and j th atom, respectively. Here, R_0 (distance between an anion and cation pair) and b (universal parameter, set to 0.37 \AA in the BondSTR program) are the empirical constants. In the present calculation, the global cutoff distance is taken to be 8 \AA at which R_0 and b are constants. The difference between

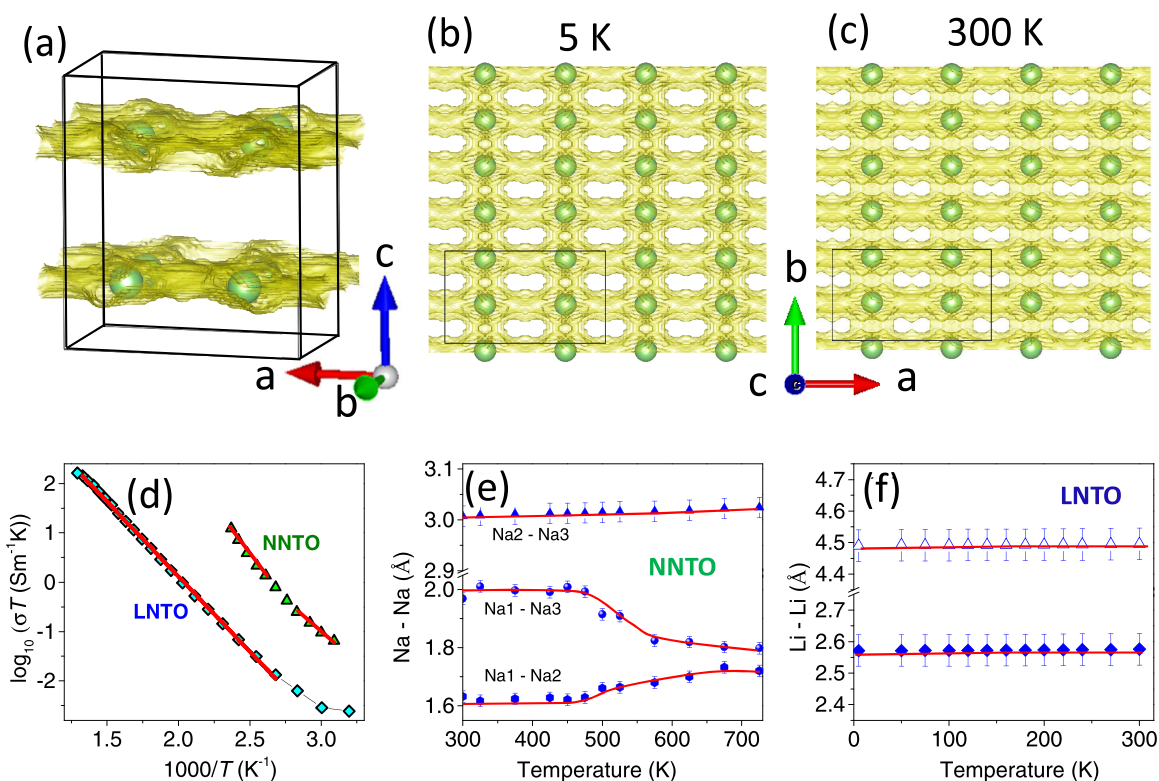


FIG. 11. (a) Bond valence (BV) map (conduction pathways) of LNTO at 300 K, represented by the yellow shaded area. The isosurface is drawn for a valence mismatch value of $\Delta V = 0.05$. Two-dimensional Li-ion conduction within the Li layers in the ab planes is evident from the shaded region. For clarity, the Li ions are shown, and other atoms (Ni, Te, and O) are omitted. Projection of the BV map in the ab plane for (b) 5 K and (c) 300 K. (d) Comparison of temperature-dependent ionic conductivity for NNTO and LNTO in Arrhenius plot. The conductivity values for NNTO are taken from Ref. [13]. Solid lines are linear fit to the data. Temperature variation of direct distances between alkali metal ions for (d) NNTO and (e) LNTO. Solid lines in (e) and (f) are guides to the eye.

the actual valence value (V_i) and the ideal value (V_0) is known as a bond valence mismatch $\Delta V = V_i - V_0$. The pathways were calculated for the valence mismatch value $\Delta V = 0.05$ valence unit (v.u.) for which an infinite network of conduction pathways occurs. The analysis reveals 2D Li-ion conduction pathways within the ab planes [Fig. 11(a)] like that reported for NNTO [13]. It is apparent that the conduction of the Li ions is not allowed along the c axis through the Ni/TeO₆ transition metal layers. The Li-ion conduction pathways within the ab planes are shown in Figs. 11(b) and 11(c) for 5 and 300 K, respectively. However, no temperature-dependent observable changes have been found in the conduction pathways. It may be highlighted that the conduction pathways within the 2D ab plane are different in these two compounds. This may be attributed due to the difference in the in-plane arrangements of the alkali metals as well as the oxygen environments around the alkali metals.

IV. DISCUSSION

Now we briefly discuss the unique features of the crystal structures of $A_2Ni_2TeO_6$ ($A = Na/Li$) and their decisive role on high ionic conductivity. Due to the layered crystal structure of $A_2Ni_2TeO_6$, the alkali metal ions reside alone within the layers, which allows alkali Na/Li ions to move without scattering from any other atom/ion within the layer. This results in high ionic conductivity even at room temperature. Although NNTO and LNTO are the isoformula compounds, their crystal structures are different (space group $Cmca$ for LNTO and space group $P6_3/mcm$ for NNTO). In NNTO, the alkali Na ions reside in a trigonal prismatic environment, whereas in LNTO, the Li ions reside in a tetrahedral environment. Figure 11(d) shows a comparative plot of the temperature dependence of ionic conductivity for both compounds LNTO and NNTO (NNTO results are taken from Ref. [13]). Although Li is lighter than Na, NNTO exhibits higher ionic conductivity ($\sigma T \sim 10^{-1} \text{ Sm}^{-1}\text{K}$ at $\sim 300 \text{ K}$) than that for the LNTO compound ($\sigma T \sim 2 \times 10^{-3} \text{ Sm}^{-1}\text{K}$ at 300 K) [Fig. 11(d)]. The differences in their conductivity values reflect the individual characteristic of the transport of charge carriers led by different crystal structural environments around the alkali metal ions. The different crystal structures, in terms of difference in the distance between the alkali ions, atomic packing density, electropotential landscape, etc., are directly related to the ionic conduction. In NNTO, the distances between the Na ions are smaller (Na1-Na2 $\sim 1.615 \text{ \AA}$ and Na1-Na3 $\sim 1.969 \text{ \AA}$ at 300 K) [Fig. 11(e)] than that for the Li ions (Li-Li $\sim 2.572 \text{ \AA}$) in LNTO [Fig. 11(f)]. The smaller distances between the Na ions leads to an easy transport of Na ions and hence results in higher ionic conductivity. The BVS analysis reveals that the Na ions which reside in Na1 and Na2 sites contribute to the ionic conduction at room temperature by making a continuous pathway through the Na1 and Na2 sites [13]. With increasing temperature above $\sim 550 \text{ K}$, the additional conduction pathways occur through the Na3 ions [13]. On the other hand, although crystal structural anomalies at $\sim 200\text{--}300 \text{ K}$ were found for LNTO, no change in the Li-Li distances occurs over the temperature range $5\text{--}300 \text{ K}$ [Fig. 11(f)]. Consequently, no change in the nature of the conduction pathways has been observed for

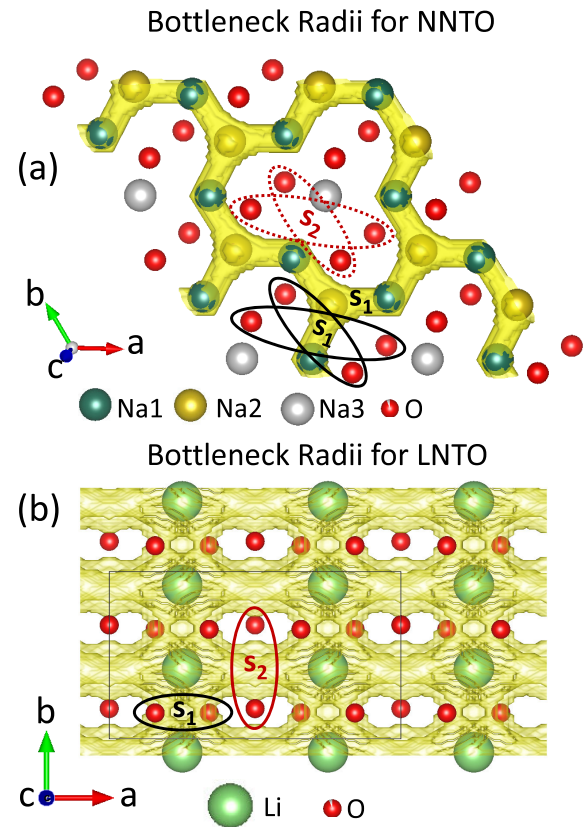


FIG. 12. Bottleneck radii for the A-ion conduction pathways in (a) NNTO and (b) LNTO.

LNTO across $200\text{--}300 \text{ K}$ [Figs. 11(b) and 11(c)]. Here, we would like to mention that we have observed high values of the thermal parameters (Biso) for Na/Li ions in the studied $A_2M_2TeO_6$ ($A = Na/Li$) compounds as compared with other atoms present in the crystal structure, viz., Ni, Te, and O. This divulges that Na/Li ions have shallow potential wells which are responsible for fast and high ionic conduction.

To further emphasize the role of the conduction pathways on the ionic conductivity, we have determined the bottleneck radius for the individual pathways. Here, the *bottleneck radius* is defined as the smallest distance between the conducting A ion and the surrounding oxygen ions at the narrowest point of a conduction pathway (as defined in Ref. [12]). For the compound NNTO, the bottleneck radius for the conduction pathway Na1-Na2 ($\sim 2.33 \text{ \AA}$) is widest among the $A_2M_2TeO_6$ series of compounds [Fig. 12 and Table I], which leads to the highest conductivity. The Na3 site does not contribute to the ionic conductivity at room temperature, which can be attributed to the relatively smaller bottleneck radius for the conduction pathway Na1-Na3 ($\sim 2.25 \text{ \AA}$ at 300 K). However, with the increase of temperature, the increase of the bottleneck radius ($\sim 2.30 \text{ \AA}$ at 725 K) along with a reduction in the distance between the Na1-Na3 atoms [Fig. 11(e)] leads to a conduction pathway through the Na3 ions. On the other hand, the bottleneck radii of LNTO (~ 1.72 and $\sim 1.9 \text{ \AA}$ for Li-Li) are wider than that for several other Li based layered honeycomb compounds [11]. This is consistent with the observed highest ionic conductivity for LNTO among them. The above

TABLE I. A comparison of bottleneck radii for the A-ion conduction pathways in the $A_2M_2TeO_6$ compounds.

Compounds	Bottleneck radius		σ (S/m) at 300 K	σ (S/m) at 573 K
	(Na1-Na2)	(Na1-Na3)		
$Na_2Zn_2TeO_6$	2.28 Å	2.29 Å	9×10^{-3} [12]	5.1–7.0 [12]
$Na_2Co_2TeO_6$	2.31 Å	2.32 Å	3.8×10^{-4} to 4.9×10^{-4} [12]	3.1–4.4 [12]
$Na_2Ni_2TeO_6$	2.33 Å(s_1)	2.25 Å(s_2)	8×10^{-4} to 34×10^{-4} [12]	10.1–10.8 [12]
$Li_2Ni_2TeO_6$	(Li-Li)		7.8×10^{-6}	25×10^{-3}
	1.722 Å(s_1) and 1.9 Å(s_2)		This paper	This paper

discussion reveals that the local arrangements of alkali metal ions play a significant role in ionic conduction.

The ion dynamics of Na/Li ions in a battery material strongly depends on Na/Li-ion occupancies, i.e., fully filled or partially filled Na/Li crystallographic sites. In a Na/Li-ion-deficient phase (having site occupancy less than its full capacity), the conducting ions jump from their original positions to the adjacent vacant regular sites. On the other hand, in a compound with fully filled Na/Li sites (i.e., up to its maximum site capacity), Na/Li ions can only jump to vacant interstitial sites. For the $Na_2Ni_2TeO_6$ compound, having space group $P6_3/mcm$, there are six positions available per formula unit in the crystal structure for the two Na^+ ions to occupy. There are 2 f.u. per unit cell where the four Na ions are distributed over Na1 (6g), Na2 (4c), and Na3 (2a) sites with a maximum allowed capacity of 12 ions. Therefore, there are 66% natural Na vacancies present in the stoichiometric $Na_2Ni_2TeO_6$ compound. Furthermore, analysis of the neutron diffraction pattern of the present Na-based sample [Fig. 1(a)] reveals the occupancies of 0.37(3), 0.18(1), and 0.11(1) for Na1 (6g), Na2 (4c), and Na3 (2a) sites, respectively [13]. Hence, in comparison with the stoichiometric $Na_2Ni_2TeO_6$, a deficiency of $\sim 15\%$ Na ions corresponding to $Na_{1.7}Ni_2TeO_6$ is revealed (Table S1 in the Supplemental Material [33]). Such partial site occupations ($\frac{1.7}{6}$) reveal that enough vacant sites are present in the Na layers, allowing Na-ion conduction through the empty regular Na sites. On the other hand, for the second compound with $A = Li$, having space group $Cmca$, there is a single crystallographic site (8e) for Li ions. In this case, there are 4 f.u. per unit cell with a maximum allowed occupancy of eight ions. Hence, there are two positions available per formula unit in the crystal structure for the two Li^+ ions to occupy, which means that all Li positions are fully occupied for a stoichiometric composition $Li_2Ni_2TeO_6$. In this paper, LNTO was synthesized from the as-prepared NNTO sample (having 15% Na-ion-deficient composition $Na_{1.7}Ni_2TeO_6$) by replacing Na ions by Li ions in an ion-exchange method. Therefore, it leads to a nonstoichiometric composition $Li_{1.7}Ni_2TeO_6$ for the LNTO sample as well, as confirmed by the Rietveld analysis of the measured neutron diffraction pattern (Table S2 in the Supplemental Material [33]). Therefore, the ion dynamics reported in this paper are related to the Na/Li deficiencies, which are of special importance to understand the performance of a battery material. In fact, from MD simulations, Sau and Kumar [19] reported that the NNTO compound with an optimum deficiency ($\sim 20\%$ Na^+ ions) provides the maximum ionic conductivity due to the marginal interaction between the mobile Na^+ ions. With increasing Na^+ -ion concentration beyond the optimum value

($Na_{1.6}Ni_2TeO_6$), the interaction between the mobile Na^+ ions increases; hence, the conductivity decreases. It was also reported [19] that the Na-ion conductivity is higher when the rest of the crystal structural framework remains static (i.e., the Ni, Te, and O ions are static or immobile). In fact, from the present neutron diffraction study, the B_{iso} values of Ni, Te, and O ions are found to be smaller than that for the Na as well as Li ions, which is favorable for the high Na- and Li-ion conductivity. In summary, further enhancement of the Na (Li)-ion conductivity for the present compounds may be possible by creating optimum Na (Li) vacancies and/or making the crystal structural framework (consisting of Ni, Te, and O ions) more static/rigid.

The other limiting factor for ionic conductivity is the cation mixing between the Na and transition metal layers. Due to the similar size of Ni^{2+} (ionic radius $r \sim 0.69$ Å) and Te^{6+} (ionic radius $r \sim 0.56$ Å) with that of the Li^+ ions ($r \sim 0.59$ Å), cation mixing can be expected in LNTO. Our neutron diffraction results reveal that the highest possible cation mixing in the studied compound is $\sim 4.6(8)\%$. Here, we would like to highlight that the LNTO sample prepared by the ion-exchange method (Ref. [13] and the present study) retains the layered structure like NNTO due to low/zero cation mixing. On the other hand, the literature [11] suggests that the LNTO sample prepared by the conventional solid-state reaction method contains a high degree of cation mixing, therefore resulting into a nonlayered disordered crystal structure. Here, we would like to mention that, although NNTO has been prepared by the solid-state reaction method, due to the difference in the sizes of Ni^{2+}/Te^{6+} ($r \sim 0.69/0.56$ Å) and Na^+ ($r \sim 1.02$ Å) ions, the cation mixing is not expected in NNTO. Our neutron diffraction results also ensure no cation mixing for NNTO.

In addition to high ionic conductivity, high working potential, and long-life electrodes for rechargeable batteries (as reported), the studied compounds $A_2Ni_2TeO_6$ can be used as electrolyte materials due to their high ionic conductivity. The special advantage would be their high working potential (~ 4.5 and 4 V for NNTO and LNTO, respectively), where conventional electrolytes made of organic solvents are prone to decomposition. Further, the crystal structural stability of these compounds with small thermal expansion over a wide temperature range, as established in this paper, makes these compounds suitable for battery application over extreme conditions. Here, we would like to mention that NNTO would be better for battery usage, as it depicts higher ionic conductivity along with high rate capability and high capacity retention as compared with that of LNTO.

Now we shed light on another important aspect of these 2D layered materials, i.e., their interesting magnetic

properties [12–22,29]. Due to the layered crystal structure, the magnetic exchange interactions mainly dominate within the 2D magnetic layers in the ab planes with a weak exchange coupling between the magnetic layers. Such a reduction in the magnetic dimensionality enhances quantum fluctuations. Additionally, the honeycomb arrangements of the magnetic Ni ions within the ab planes and in-plane exchange interactions between the Ni ions beyond the first nearest neighbors lead to geometrical frustrations. Such enhanced quantum fluctuations and geometrical frustrations result in unusual magnetic properties [12–22]. The compound NNTO has been studied extensively for its interesting magnetic properties. The alkali metal Na ions that are sandwiched between the honeycomb magnetic layers not only act as a nonmagnetic separator but also dictate the magnetic symmetry of the materials [21]. Interesting coexisting commensurate (CM) long-range and incommensurate (ICM) short-range magnetic correlations were reported [21]. Further, for the CM long-range phase, an unusual up-up-down-down ($\uparrow\uparrow\downarrow\downarrow$) periodicity (along the c axis) of the in-plane antiferromagnetic (AFM) spin structure was also reported [21]. It was reported that the intermediate Na layer plays a significant role in stabilizing both coexisting CM and ICM phases as well as up-up-down-down periodicity of the CM AFM structure. On the other hand, only a preliminary experimental report on the bulk magnetic properties is available for the other compound LNTO, where the temperature-dependent susceptibility study reveals a long-range AFM ordering below ~ 24.4 K [29]. DFT calculations [29] predicted an AFM structure consisting of AFM coupled ferromagnetic chains within the honeycomb layers. Additional short-range magnetic ordering was proposed above T_N up to ~ 34 K [29]. Detailed knowledge of the magnetic ground state of LNTO could be a potential future research scope.

V. SUMMARY AND CONCLUSIONS

In summary, detailed crystal structural and electrical properties and their intercorrelations in the potential battery materials $A_2Ni_2TeO_6$ ($A = Na/Li$) have been divulged through a combined in-depth study of neutron diffraction, Raman spectroscopy, and impedance spectroscopy. For both Na- and Li-based compounds, the layered crystal structures consist of alternating stacking of $(Ni/Te)O_6$ and Na/Li-ion layers along the crystallographic c axis. The structure of the $(Ni/Te)O_6$ layers are identical in both compounds. However, the internal structures of the alkali metal layers are different, where LNTO has a LiO_4 trigonal prismatic environment in

contrast to a NaO_6 octahedral environment in NNTO. Even though Li is lighter than Na, NNTO exhibits higher ionic conductivity than the LNTO compound due to the different crystal structure environments around the alkali metal ions (distances between the Na ions are smaller in NNTO than that for the Li ions in LNTO). Further, our soft BVS analysis of the neutron diffraction pattern of LNTO reveals a 2D ionic conduction pathway like NNTO. With increasing temperature, site-specific contribution of Na-ion conduction is evident for NNTO [13], where > 550 K, in addition to the Na1 and Na2 sites, ionic conduction pathways occur involving the Na3 site as well due to the reduction of the Na1-Na3 distance > 550 K. On the other hand, due to insignificant change in the Li-Li distance, no change in the nature of the conduction pathways has been observed for LNTO. We have shown that the studied compounds exhibit a high value of ionic conductivity along with a high value of dielectric constants and low dielectric losses. Such properties are advantageous for a high-density energy storage application with low energy loss. The temperature-dependent Arrhenius behavior of ionic conductivity obtained from impedance spectroscopy reveals a thermally activated conduction process with activation energies 0.58(3) and 0.261(4) eV for NNTO and LNTO, respectively. Analysis of the temperature-dependent neutron diffraction patterns reveals that the crystal structural symmetry remains unchanged over 5–873 K, ensuring good structural stability for both compounds $A_2Ni_2TeO_6$ ($A = Na/Li$). However, local crystal structural anomalies in terms of bond lengths and bond angles are evident at ~ 475 – 575 K and ~ 200 – 300 K for NNTO and LNTO, respectively. The role of the underlying crystal structure on the electrical properties has been demonstrated for both compounds $A_2Ni_2TeO_6$ where temperature-dependent local crystal structural anomalies (bond lengths, bond angles, and polyhedral distortions) impact the electrical properties. The present in-depth understanding of the electrostructural correlations of the highly efficient layered battery materials is useful for the advancement of battery research in the field of high-density storage devices.

ACKNOWLEDGMENTS

The authors would like to acknowledge the help provided by V. B. Jayakrishnan for the x-ray diffraction measurements. B. Saha thanks the Department of Science and Technology, Government of India, for providing the INSPIRE fellowship (INSPIRE Grant No. IF180105).

-
- [1] V. Palomares, P. Serras, I. Villaluenga, K. B. Hueso, J. Carretero-González, and T. Rojo, *Energy Environ. Sci.* **5**, 5884 (2012).
 - [2] J. B. Goodenough and K.-S. Park, *J. Am. Chem. Soc.* **135**, 1167 (2013).
 - [3] X. Xiang, K. Zhang, and J. Chen, *Adv. Mater.* **27**, 5343 (2015).
 - [4] N. Nitta, F. Wu, J. T. Lee, and G. Yushin, *Mater. Today* **18**, 252 (2015).
 - [5] X. Xie, S. Wang, K. Kretschmer, and G. Wang, *J. Colloid Interface Sci.* **499**, 17 (2017).
 - [6] J. M. Tarascon and M. Armand, in *Materials for Sustainable Energy: A Collection of Peer-Reviewed Research and Review Articles from Nature Publishing Group* (World Scientific, Singapore, 2011), p. 171.
 - [7] M. Park, X. Zhang, M. Chung, G. B. Less, and A. M. Sastry, *J. Power Sources* **195**, 7904 (2010).
 - [8] K. Kubota, N. Yabuuchi, H. Yoshida, M. Dahbi, and S. Komaba, *MRS Bull.* **39**, 416 (2014).
 - [9] C. Delmas, *Adv. Energy Mater.* **8**, 1703137 (2018).

- [10] B. Saha, A. K. Bera, and S. M. Yusuf, *ACS Appl. Energy Mater.* **4**, 6040 (2021).
- [11] G. M. Kanyolo, T. Masese, N. Matsubara, C. Y. Chen, J. Rizell, O. K. Forslund, E. Nocerino, K. Papadopoulos, A. Zubayer, M. Kato *et al.*, *Chem. Soc. Rev.* **50**, 3990 (2021).
- [12] M. A. Evstigneeva, V. B. Nalbandyan, A. A. Petrenko, B. S. Medvedev, and A. A. Kataev, *Chem. Mater.* **23**, 1174 (2011).
- [13] A. K. Bera and S. M. Yusuf, *J. Phys. Chem. C* **124**, 4421 (2020).
- [14] A. I. Kurbakov, A. N. Korshunov, S. Y. Podchezertsev, M. I. Stratan, G. V. Raganyan, and E. A. Zvereva, *J. Alloys Compd.* **820**, 153354 (2020).
- [15] S. K. Karna, Y. Zhao, R. Sankar, M. Avdeev, P. C. Tseng, C. W. Wang, G. J. Shu, K. Matan, G. Y. Guo, and F. C. Chou, *Phys. Rev. B* **95**, 104408 (2017).
- [16] R. Sankar, I. P. Muthuselvam, G. Shu, W. Chen, S. K. Karna, R. Jayavel, and F. Chou, *CrystEngComm* **16**, 10791 (2014).
- [17] A. Gupta, C. B. Mullins, and J. B. Goodenough, *J. Power Sources* **243**, 817 (2013).
- [18] Y. Itoh, *J. Phys. Soc. Jpn.* **84**, 064714 (2015).
- [19] K. Sau and P. P. Kumar, *J. Phys. Chem. C* **119**, 18030 (2015).
- [20] A. Korshunov, I. Safiulina, and A. Kurbakov, *Phys. Status Solidi* **257**, 1900232 (2020).
- [21] A. Bera, S. M. Yusuf, L. Keller, F. Yokaichiya, and J. R. Stewart, *Phys. Rev. B* **105**, 014410 (2022).
- [22] J. Pati, H. Raj, S. K. Sapra, A. Dhaka, A. K. Bera, S. M. Yusuf, and R. S. Dhaka, *J. Mater. Chem. A* **10**, 15460 (2022).
- [23] M. Medarde, M. Mena, J. L. Gavilano, E. Pomjakushina, J. Sugiyama, K. Kamazawa, V. Yu. Pomjakushin, D. Sheptyakov, B. Batlogg, H. R. Ott *et al.*, *Phys. Rev. Lett.* **110**, 266401 (2013).
- [24] Z. Ma, Y. Wang, C. Sun, J. Alonso, M. Fernández-Díaz, and L. Chen, *Sci. Rep.* **4**, 7231 (2014).
- [25] K. Sau and P. P. Kumar, *J. Phys. Chem. C* **119**, 1651 (2015).
- [26] V. Kumar, N. Bhardwaj, N. Tomar, V. Thakral, and S. Uma, *Inorg. Chem.* **51**, 10471 (2012).
- [27] N. S. Grundish, I. D. Seymour, G. Henkelman, and J. B. Goodenough, *Chem. Mater.* **31**, 9379 (2019).
- [28] V. Kumar, A. Gupta, and S. Uma, *Dalton Trans.* **42**, 14992 (2013).
- [29] T. Vasilchikova, A. Vasiliev, M. Evstigneeva, V. Nalbandyan, J.-S. Lee, H.-J. Koo, and M.-H. Whangbo, *Materials* **15**, 2563 (2022).
- [30] J. Rodríguez-Carvajal, *Physica B* **192**, 55 (1993).
- [31] J. Rodríguez-Carvajal, *Bond_Str* (2010), http://mill2.chem.ucl.ac.uk/ccp/web-mirrors/plotr/BondStr/Bond_Str.htm.
- [32] K. Momma and F. Izumi, *J. Appl. Cryst.* **44**, 1272 (2011).
- [33] See Supplemental Material at <http://link.aps.org/supplemental/10.1103/PhysRevMaterials.7.085001> for details on crystal structural parameters at room temperature as well as temperature dependence of Raman spectra and Raman mode frequencies for $A_2Ni_2TeO_6$ ($A = Na/Li$) compounds; also contains Ref. [28].
- [34] J. Paulsen, R. Donaberger, and J. Dahn, *Chem. Mater.* **12**, 2257 (2000).
- [35] H. Xiang, L. Fang, W. Fang, Y. Tang, and C. Li, *J. Eur. Ceram. Soc.* **37**, 625 (2017).
- [36] J. M. Jehng and I. E. Wachs, *Chem. Mater.* **3**, 100 (1991).
- [37] S. K. Singh and V. R. K. Murthy, *Mater. Chem. Phys.* **160**, 187 (2015).
- [38] P. Rosaiah and O. Hussain, *Adv. Mater. Lett* **4**, 288 (2013).
- [39] M. Prabu, S. Selvasekarapandian, A. Kulkarni, S. Karthikeyan, G. Hirankumar, and C. Sanjeeviraja, *Ionics* **17**, 201 (2011).
- [40] M. Ram and S. Chakrabarti, *J. Alloys Compd.* **462**, 214 (2008).
- [41] N. Murali, S. J. Margarete, V. K. Rao, and V. Veeraiah, *J. Sci.: Adv. Mater. Devices* **2**, 233 (2017).
- [42] S. Badhwar, D. Maurya, and J. Kumar, *J. Mater. Sci. Mater. Electron.* **16**, 495 (2005).
- [43] P. Gupta and P. Poddar, *RSC Adv.* **5**, 10094 (2015).
- [44] R. N. Bhowmik and A. G. Lone, *J. Alloys Compd.* **680**, 31 (2016).
- [45] X. He, Y. Zhu, and Y. Mo, *Nat. Commun.* **8**, 15893 (2017).
- [46] K. Funke, *Solid State Ionics* **94**, 27 (1997).
- [47] H. Wu and F. Li, *Phys. Lett. A* **383**, 210 (2019).
- [48] N. J. De Klerk and M. Wagemaker, *Chem. Mater.* **28**, 3122 (2016).
- [49] S.-H. Bo, Y. Wang, J. C. Kim, W. D. Richards, and G. Ceder, *Chem. Mater.* **28**, 252 (2016).
- [50] R. Schlem, A. Banik, M. Eckardt, M. Zobel, and W. G. Zeier, *ACS Appl. Energy Mater.* **3**, 10164 (2020).
- [51] S. Adams and J. Swenson, *Solid State Ionics* **154**, 151 (2002).
- [52] S. Adams and R. P. Rao, *Phys. Status Solidi* **208**, 1746 (2011).
- [53] D. R. Bhosale, S. M. Yusuf, A. Kumar, M. D. Mukadam, and S. I. Patil, *Phys. Rev. Mater.* **1**, 015001 (2017).